



저작자표시-비영리-변경금지 2.0 대한민국

이용자는 아래의 조건을 따르는 경우에 한하여 자유롭게

- 이 저작물을 복제, 배포, 전송, 전시, 공연 및 방송할 수 있습니다.

다음과 같은 조건을 따라야 합니다:



저작자표시. 귀하는 원저작자를 표시하여야 합니다.



비영리. 귀하는 이 저작물을 영리 목적으로 이용할 수 없습니다.



변경금지. 귀하는 이 저작물을 개작, 변형 또는 가공할 수 없습니다.

- 귀하는, 이 저작물의 재이용이나 배포의 경우, 이 저작물에 적용된 이용허락조건을 명확하게 나타내어야 합니다.
- 저작권자로부터 별도의 허가를 받으면 이러한 조건들은 적용되지 않습니다.

저작권법에 따른 이용자의 권리는 위의 내용에 의하여 영향을 받지 않습니다.

이것은 [이용허락규약\(Legal Code\)](#)을 이해하기 쉽게 요약한 것입니다.

[Disclaimer](#)

Master's Thesis

Improved cycling performance of high capacity
spinel cathode material for Li-ion batteries

Eunsol Lho

Department of Energy Engineering
(Battery Science and Technology)

Graduate School of UNIST

2016

Improved cycling performance of high capacity spinel cathode material for Li-ion batteries

Eunsol Lho

Department of Energy Engineering
(Battery Science and Technology)

Graduate School of UNIST

Improved cycling performance of high capacity spinel cathode material for Li-ion batteries

A thesis/dissertation
submitted to the Graduate School of UNIST
in partial fulfillment of the
requirements for the degree of
Master of Science

Eunsol Lho

1. 13. 2016

Approved by



Advisor

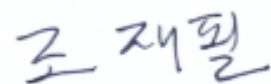
Jaephil Cho

Improved cycling performance of high capacity
spinel cathode material for Li-ion batteries

Eunsol Lho

This certifies that the thesis/dissertation of Eunsol Lho is approved.


1. 13. 2016



Advisor: Jaephil Cho



Youngsik Kim



Yoon seok Jung

Contents

Abstract-----	i
List of figures-----	ii
List of tables-----	iii
I . Introduction -----	1
1.1 Lithium-ion batteries-----	1
1.2 Spinel LiMn_2O_4 cathode material for lithium ion batteries-----	3
1.2.1 Spinel structure-----	5
1.2.2 Advantages of spinel-----	6
1.2.3 Causes of capacity fading at the elevated temperature-----	7
1.2.3-1 Mn dissolution -----	8
1.2.3-2 Oxygen deficiency -----	10
1.2.3-3 Jahn-Teller distortion -----	13
1.2.4 Strategies to improve the cycling performance-----	15
II . Experiment-----	19
2.1 Experimental method-----	19
2.2 Electrochemical measurement-----	19
2.3 Instrumental analysis-----	20
III. Results and discussions-----	21
IV. Conclusion-----	42
V . References-----	43
VI. Acknowledgements-----	50

Abstract

In the face of growing clean energy needs and strengthened environmental regulations, Lithium ion batteries (LIBs) are spotlighted as the sustainable energy alternatives. Recently, with growing interest in electric vehicles and energy storage systems, large scale batteries are focused. For these large scale applications of LIBs, many researchers have attempted to develop the cathode material with high thermal stability, excellent cycling retention, low cost, high power and energy density.

The mostly used cathode materials in the early commercialized EVs are the low portion of Ni-rich layered and the high portion of cation-doped spinel material composite. The reason why the spinel is more proper is that it has many advantages of low cost, abundance, nontoxicity and good thermal stability, which is suitable for requirement of EVs. However, it also has serious problem of manganese dissolution in elevated temperatures. Thus, the portion of Ni-rich layered material (170 mAh g^{-1}) is raised to increase driving range recently. However, the changing composition of cathode materials causes increasing battery cost resulting in the hindrance of widely commercializing EVs because the price of Ni-rich materials is approximately 3 times higher than that of spinel material. Therefore, the spinel cathode material toward high stability and capacity ($>120 \text{ mAh g}^{-1}$) should be developed.

In this paper, we tried to develop high capacity and high stability spinel material for EVs. We synthesized Al doped spinel as bare and optimized it for the best cycling performance. The discharge capacity of this optimized bare was 125.4 mAh g^{-1} and the cycling retention after 100cycles at 60°C was 82.2% of its initial capacity. And then we proceed with coating and doping simultaneously. The coating layer can protect the surface of bare from being directly exposed to the HF in electrolyte and suppress the dissolution of Mn ions. Also fluorine is doped into vacant oxygen site on the surface for structural stability. Accordingly, the cycle performance at elevated temperature is significantly improved. This coated LiMn_2O_4 exhibited a discharge capacity of 120.1 mAh g^{-1} and retained 94% of its initial capacity at 60°C after 100 cycles.

List of figures

Figure 1. Past, present and forecast of the world's energy needs up to 2050

Figure 2. Comparison of the different battery technologies in terms of volumetric and gravimetric energy density

Figure 3. Trend of cathode materials used in LIBs

Figure 4. Schematic of atomic structure of spinel

Figure 5. Li diffusion path in spinel LiMn_2O_4

Figure 6. Mechanisms of Mn^{3+} dissolution

Figure 7. Schematic presentation the irreversible Li ion loss by Mn reduction at anode surface

Figure 8. Structure of oxygen-deficient spinel

Figure 9. Charge/discharge curve of $\text{Li}_{1.002}\text{Mn}_{1.998}\text{O}_{3.981}$

Figure 10. (a) TEM image of LiMn_2O_4 particles. (b) STEM image of the edge of a typical LiMn_2O_4 particle. The arrow indicates the region of the EELS line scan. (c) Integrated intensity of the Mn-L2,3, O-K, Mn-M2,3 and Li-K edges. (d) ELNES of Mn-M2,3 and Li-K showing the difference in Li concentration between the center and surface regions, as well as the chemical shift of Mn-M2,3. (e) ELNES of O-K edge showing the differences in pre-peak height and main peak position between the center and surface regions. (f) ELNES of the Mn-L2,3 edge showing a chemical shift from the center to the surface region

Figure 11. Upper panel: crystal-field splitting of five-fold degenerate atomic 3d levels into lower t_{2g} (triply degenerate) and higher e_g (doubly degenerate) levels. Jahn-Teller distortion of MnO_6

Figure 12. Open circuit voltage of $\text{Li}_x\text{Mn}_2\text{O}_4$ as a function of x ; (I) cubic LiMn_2O_4 and cubic Mn_2O_4 , (II) cubic $\text{Li}_x\text{Mn}_2\text{O}_4$ and (III) tetragonal $\text{Li}_2\text{Mn}_2\text{O}_4$ and cubic LiMn_2O_4

Figure 13. Specific discharge capacities vs. cycle number of $\text{LiAl}_x\text{Mn}_{2-x}\text{O}_4$ electrodes cycled between 3.4 and 4.3 $\text{V}_{\text{Li}/\text{Li}^+}$ (a) 25 and (b) 45°C

Figure 14. Cyclability data of (a) LiMn_2O_4 , (b) $\text{LiCo}_{0.5}\text{Ni}_{0.5}\text{O}_2$ -modified LiMn_2O_4 , (c) LiCoO_2 -modified LiMn_2O_4 , (d) $\text{Li}_{0.75}\text{CoO}_2$ -modified LiMn_2O_4 , and (e) Al_2O_3 -modified LiMn_2O_4 at a current density of $0.5\text{mA}/\text{cm}^2$ (C/2 rate) at 60°C

Figure 15. X-ray diffraction patterns for BLMO (black) and FLMO (red)

Figure 16. SEM images of BLMO (a,b,c) and FLMO (d,e,f) particles

Figure 17. SEM images of FLMO and EDX mapping for Mn, Ni and Co

Figure 18. Mn 2p X-ray photoelectron spectroscopy (XPS) spectra of (a) BLMO and (b) FLMO

Figure 19. (a) STEM images of FLMO, (b) Structural scheme of the region A; Spinel structure viewed along the cubic [110] direction (c) Structural scheme of the region B; Layered structure viewed along the hexagonal $[2\bar{2}1]$ direction.

Figure 20. (a) TEM images of FLMO (b) Distribution of F element (wt%) in five pointed areas in the FLMO of figure (a)

Figure 21. First charge/discharge profiles of the BLMO(black) and FLMO(red) at 0.1C rate in lithium-ion half-cells (2032R-type) at 24 °C

Figure 22. Electrochemical characteristics of the BLMO(black) and FLMO(red) at 24 °C; (a) discharge rate capability tested between 3.0V-4.3V at 0.5C charge rate and with an increasing discharge C-rate to 10C. (b) charge rate capability tested between 3.0V-4.3V at 0.5C discharge rate and with an increasing charge C-rate to 10C

Figure 23. Initial discharge voltage profiles of the (a)BLMO and (b)FLMO materials at rates of 1, 3, 5, 7 and 10C, initial charge voltage profiles of the (c)BLMO and(d)FLMO materials at rates of 1, 3, 5, 7 and 10C

Figure 24. Discharge profiles of (a) BLMO and (b) FLMO as a function of temperatures at 0.1 C rate

Figure 25. (a) The proposed equivalent circuit used for analyzing the impedance patterns. Nyquist plot for (b)BLMO and FLMO in regard to after formation

Figure 26. Cycling performances of the BLMO(black) and FLMO(red) in lithium-ion half-cells(2032R-type) at 60 °C

Figure 27. Cycling performances of the Stoichiometric LiMn_2O_4 (black), $\text{Li}_{1.02}\text{Mn}_{1.98}\text{O}_4$ (red), $\text{Li}_{1.01}\text{Al}_{0.03}\text{Mn}_{1.96}\text{O}_4$ (blue) and $\text{Li}_{1.01}\text{Al}_{0.06}\text{Mn}_{1.93}\text{O}_4$ (magenta, denoted as BLMO)in lithium-ion half-cells(2032R-type) at 60 °C

Figure 28. Cycling performances of the BLMO(black), FLMO(red) and coated sample without F doping (blue) in lithium-ion half-cells(2032R-type) at 60 °C

Figure 29. Mn dissolution for the electrolyte of the fully charged (to 4.3V) Li/BLMO and Li/FLMO cells during 6weeks at 60 °C

Figure 30. The discharge voltage profile of the (a) BLMO(black) and (b)FLMO(red) stored at 60 °C for 2 weeks in fully-charged state of 4.3V

Figure 31. Nyquist plot for (a) BLMO, and (b) FLMO with respect to cycle numbers: 1st, 50th, 100th cycles.

Figure 32. (a) Ex-situ XRD patterns of BLMO; before(black), after 100cycles(red), after 200cycles(blue) at 60 °C (b) Ex-situ XRD patterns of FLMO; before(black), after 100cycles(red), after 200cycles(blue) at 60 °C

Figure 33. (a) Plot of difference in lattice parameter for samples after 100cycles(black) and 200 cycles(red) at 60 °C (b) Plot of difference in FWHM based on (311) diffraction line for samples after

100cycles(black) and 200 cycles(red) at 60°C

Figure 34. The SEM images of BLMO a) and FLMO b), particles after 100cycles at 60°C. The FIB-SEM images of the BLMO (c, e) and FLMO (d, f) after 100cycles at 60°C.

List of tables

Table 1. Characterization of BLMO and FLMO

Table 2. The diffusivity of BLMO and FLMO

Table 3. The lattice parameter and the volume of the BLMO and FLMO

I . Introduction

1.1 Lithium-ion batteries

In the face of growing clean energy needs and strengthened environmental regulations, Lithium ion batteries (LIBs) are spotlighted as the sustainable energy alternatives. Energy storage technology is more significant than before. As shown in figure 1, the world's energy need is being increased. In the past, small sized LIBs for portable electronic devices such as mobile phones and laptop computers are usually used. But these days with growing interest in electric vehicles and energy storage systems, medium and large scale batteries are focused. Therefore many researchers have attempted to develop the cathode material with high thermal stability, excellent cycling retention, low cost, high power and energy density.

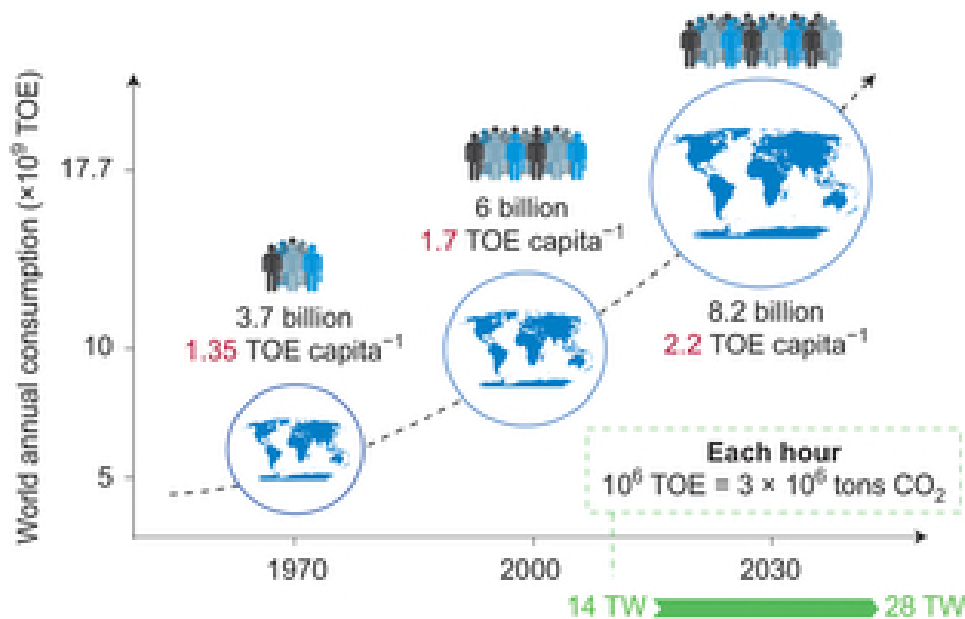


Figure 1. Past, present and forecast of the world's energy needs up to 2050 ¹.

Recently the research of large scale LIBs is mainly in progress and it receives much attention from the specific commercial fields such as electric vehicles (EVs), Hybrid electric vehicles (HEVs) and energy storage systems (ESSs). LIBs are high energy/power density, stable cyclability, safety, reasonable price and no memory effect. (figure2)

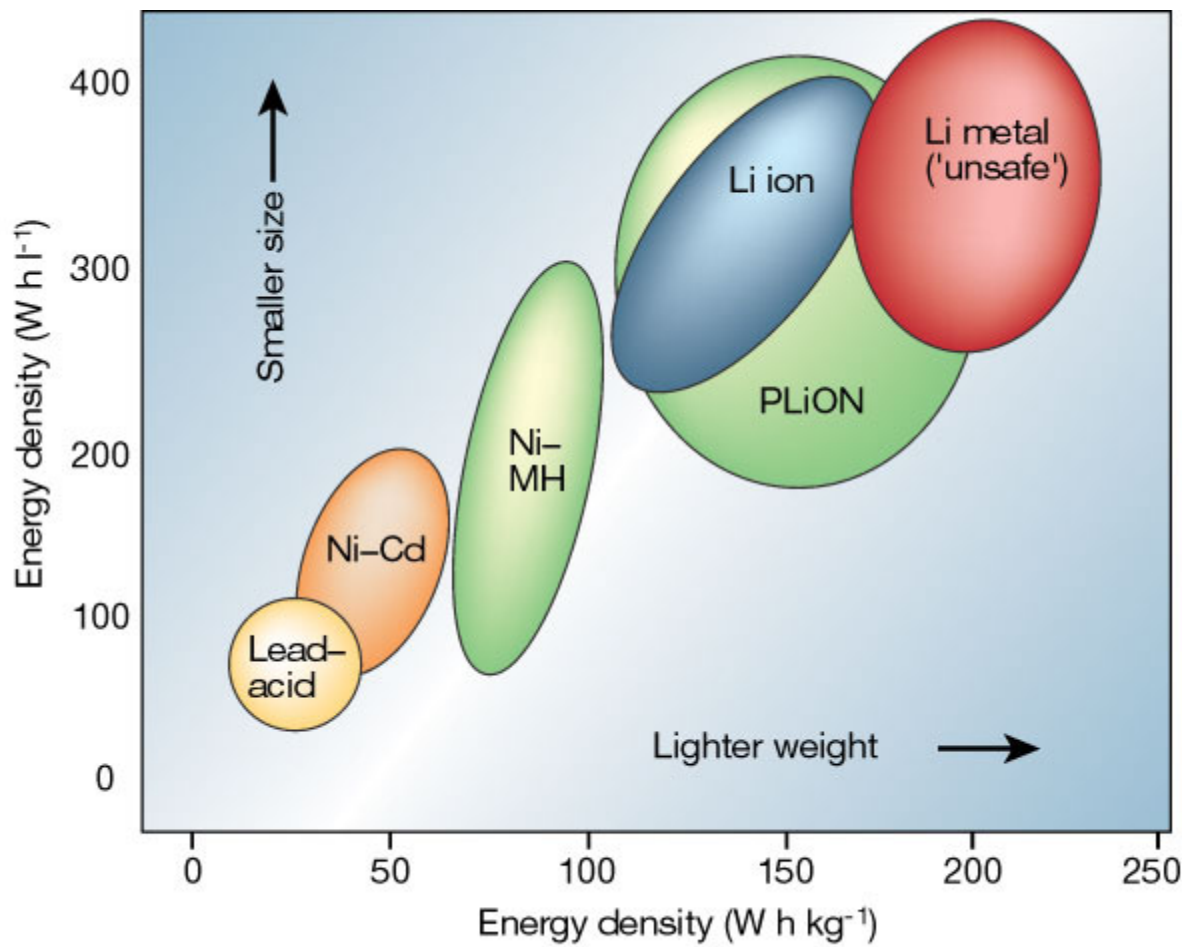


Figure 2. Comparison of the different battery technologies in terms of volumetric and gravimetric energy density ².

1.2 Spinel LiMn_2O_4

Many cathode materials have been extensively developed such as layered (LiMO_2 , $M=\text{Co}$, Al , Mn and Ni etc.), spinel (LiMn_2O_4) and olivine (LiMPO_4 , $M=\text{Fe}$, Mn and Co etc.) cathode materials since the lithium ion batteries were launched in commercial markets¹⁴. Among them, LiCoO_2 (LCO) having layered structure is the most popular cathode material and practically used in the batteries for mobile devices, because of its advantages of high energy density, lower side reactions on surface and stable cycling performance at room temperature. However, it also suffers from high cost and safety issues, therefore, the LCO is unqualified for large scale batteries to be used for EVs due to the above reasons.

The mostly used cathode materials in the early commercialized EVs are the low portion of Ni-rich layered and the high portion of cation-doped spinel material composite. The reason of why the spinel is more proper is that it has many advantages of low cost, abundance, nontoxicity and good thermal stability, which is suitable for requirement of EVs. However, it also has serious problem of manganese dissolution in elevated temperatures. To solve this issue, the cations such as Mg , Al , Li , Ni and so on are doped in spinel structure leading to increasing stability, but decreasing specific capacity around 105 mAh g^{-1} . Thus, the portion of Ni-rich layered material (170 mAh g^{-1}) is raised to increase driving range recently. However, the changing composition of cathode materials causes increasing battery cost resulting in the hindrance of widely commercializing EVs because the price of Ni-rich materials is approximately 3 times higher than that of spinel material. Therefore, the spinel cathode material toward high stability and capacity ($>120 \text{ mAh g}^{-1}$) should be developed.

Due to EVs, large scaled LIBs are new trend. The development of cathode materials for EVs has emerged. In the recent year, a spinel lithium manganese oxide (LiMn_2O_4) has taken center stage as the most promising cathode material for high power LIBs because of its low cost, abundance, nontoxicity, good thermal stability, high operating voltage and excellent rate capability. The trend of cathode materials used in LIBs is displayed in figure 3. The amount of spinel lithium manganese oxide (LiMn_2O_4) used in LIBs is gradually increased.

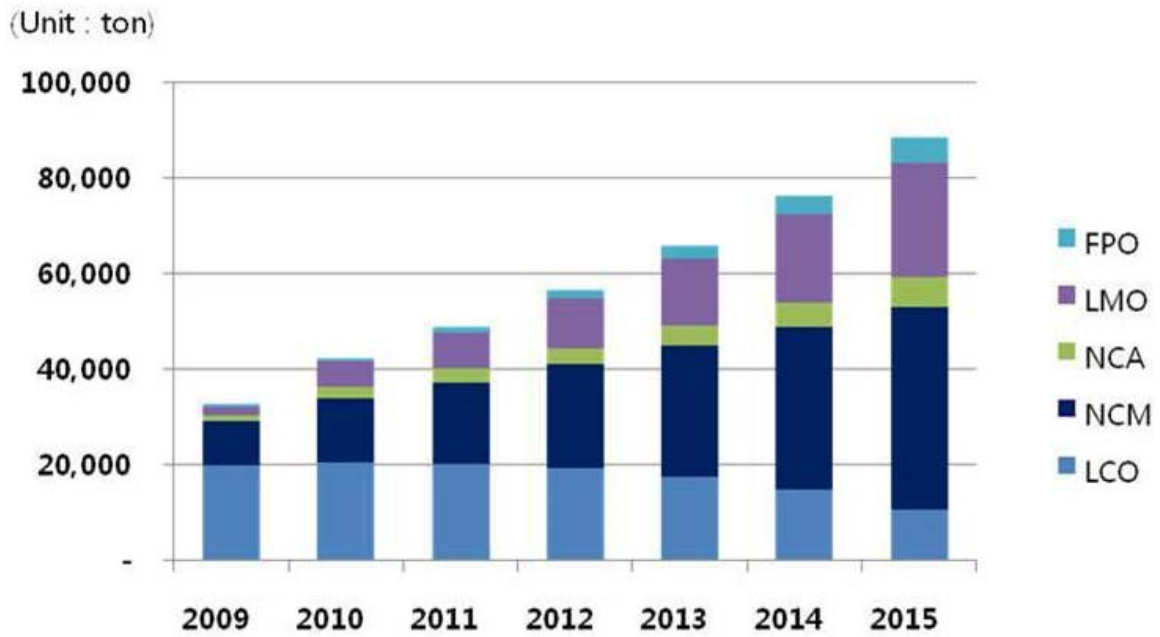


Figure 3. Trend of cathode materials used in LIBs ³.

1.2.1 Spinel structure

The structural features of the spinel largely influence the electrochemical performances. Figure 4 shows the crystal structure of cubic spinel LiMn_2O_4 (space group : $Fd-3m$). Oxygen are stacked by FCC(Face Centered Cubic). The Oxygen ions present on the 32e site. 32 octahedral and 64 tetrahedral interstices exist between the anions in the cubic unit cell. Mn ions are coordinated with oxygen ions. 3-D network is formed sharing MnO_6 -octahedra (16d sites) and Li ions are located in the tetrahedral sites. So, Li and Mn ions occupy 1/8 of the tetrahedral sites and 1/2 of the octahedral sites respectively. Some tetrahedral sites called 8b and octahedral sites called 16c are vacant. ¹⁵

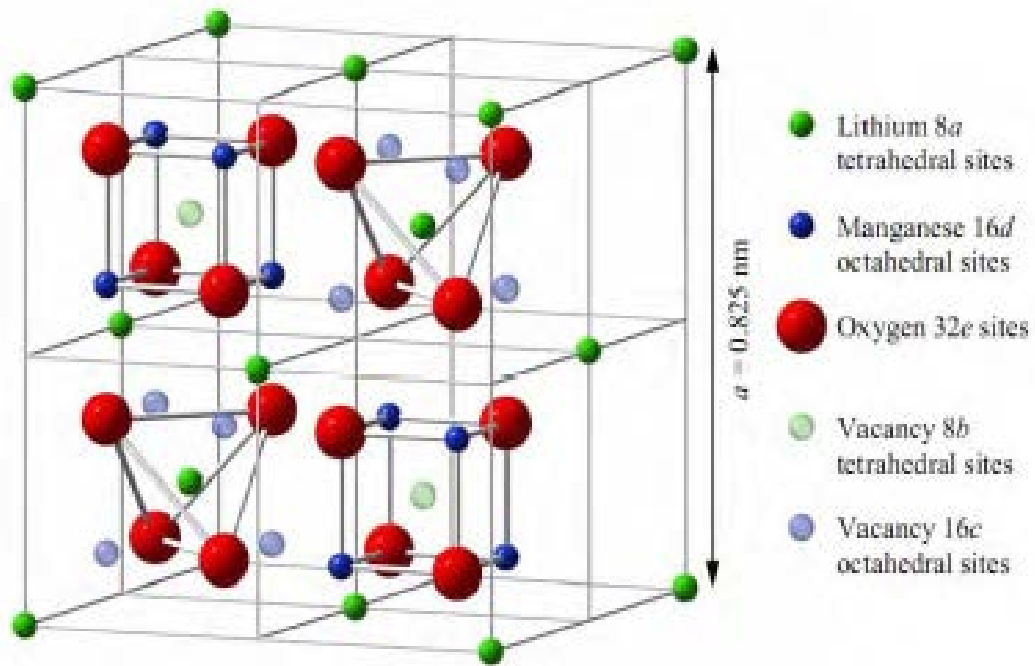


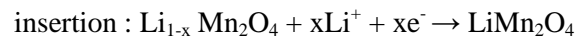
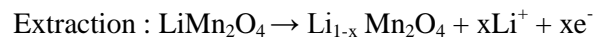
Figure 4. Schematic of atomic structure of spinel ⁶.

1.2.2 Advantages of spinel

Spinel LiMn_2O_4 (LMO) is a very promising material for LIBs because its low cost, abundance, nontoxicity, good thermal stability, high operating voltage and excellent rate capability.

There are occupied tetrahedral sites (8a) and unoccupied octahedral sites (16c) in M_2O_4 framework. These form diamond-like 3D tunnel for lithium ions. As shown in figure 5, during electrochemical reaction, the Li ions diffuse by hopping along the 3D diffusion pathway of 8a-16c-8a-16c-8a- mechanism in LiMn_2O_4 spinel¹¹. This 3D diffusion pathway in spinel leads to delivering fast lithium ion insertion/extraction. Due to its many advantages, spinel LiMn_2O_4 (LMO) is spotlighted as the cathode material for largescale batteries.

The average oxidation state of Mn ions in LiMn_2O_4 is +3.5. Extraction/ insertion of lithium ions occur from/into the λ - Mn_2O_4 host lattice. A reversible $\text{Mn}^{3+}/\text{Mn}^{4+}$ redox reaction is occurred simultaneously. Spinel LiMn_2O_4 has a theoretical capacity value of 148mAh/g in voltage range from 3.0V to 4.3V. The Extraction/insertion reaction of the lithium manganese oxide occurs shown in below reactions



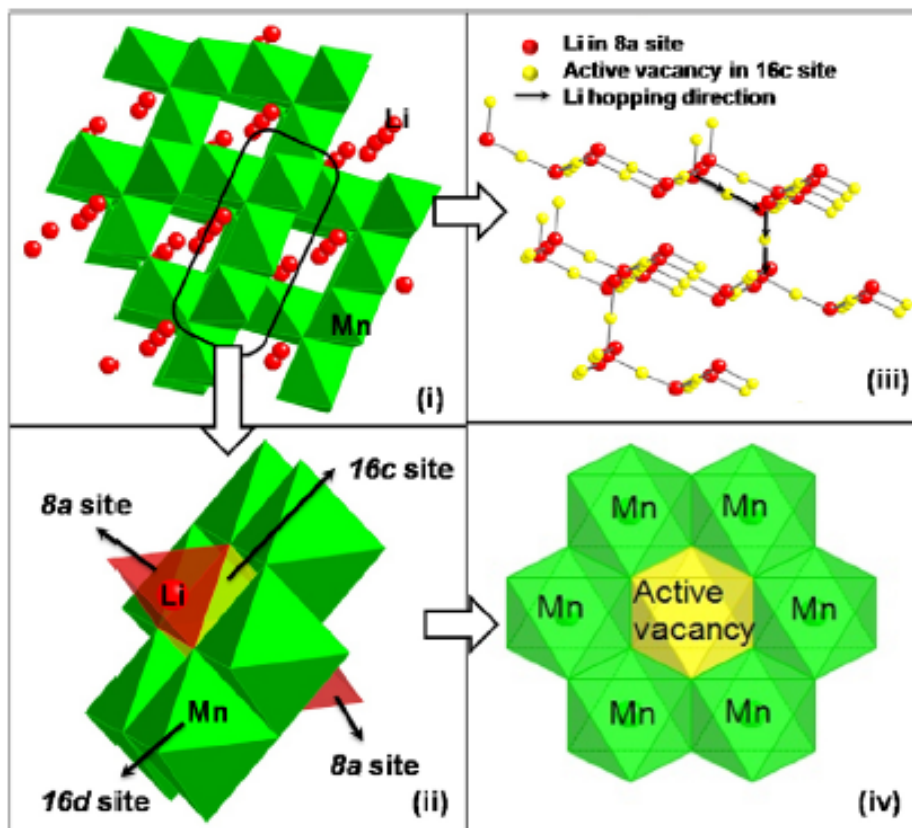


Figure 5. Li diffusion path in spinel LiMn_2O_4 ¹¹.

1.2.3 Causes of capacity fading at the elevated temperature

Though Spinel LiMn_2O_4 (LMO) is very promising cathode material for LIBs, it still has some disadvantages for application. One of these disadvantages is the severe capacity fading upon extended electrochemical cycling, especially at high temperature ($>60^\circ\text{C}$). Such a problem is caused by several reasons.

- (1) Mn^{3+} dissolution into the electrolyte ¹⁶
- (2) Oxygen deficient LiMn_2O_4 ^{7, 13, 17}
- (3) Jahn-Teller distortion of Mn^{3+} . ¹⁸

1.2.3-1 Mn³⁺ dissolution

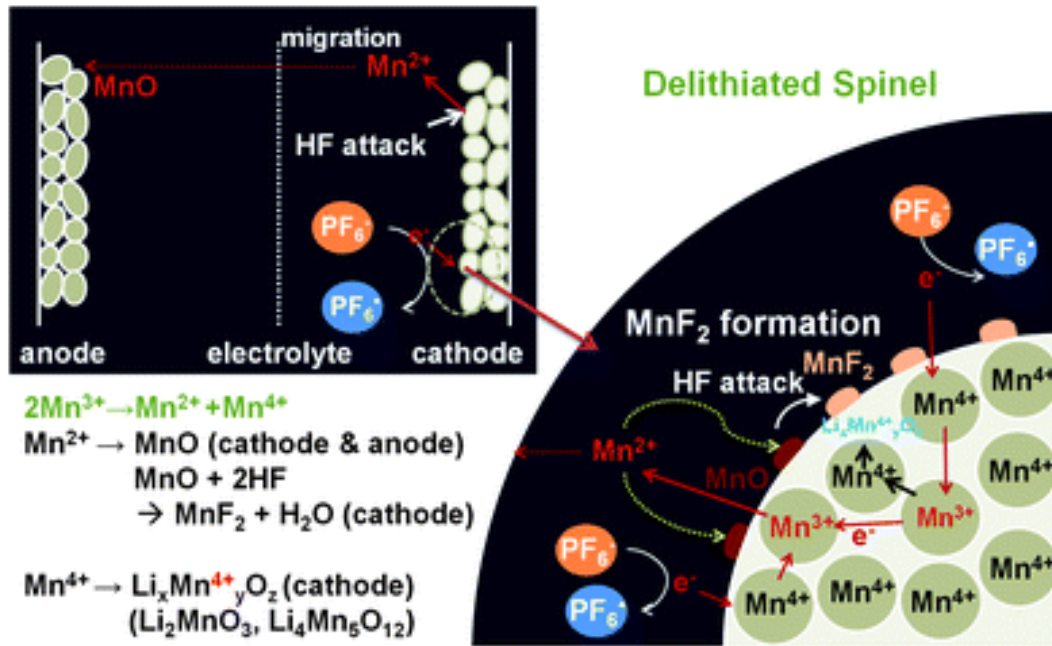
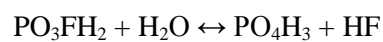
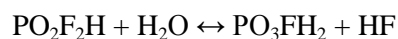
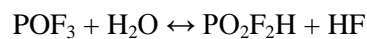
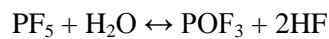
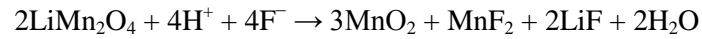


Figure 6. Mechanisms of Mn³⁺ dissolution⁴.

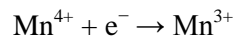
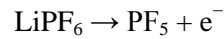
Mn dissolution is one of the main reasons causing capacity fading of LiMn₂O₄ at elevated temperature. The Mn dissolution reactions are as shown in figure 6. Two possible Mn³⁺ dissolution mechanisms ($2\text{Mn}^{3+}_{\text{solid}} \rightarrow \text{Mn}^{4+}_{\text{solid}} + \text{Mn}^{2+}_{\text{solution}}$) have been proposed in figure 6. It is suggested that surface water molecules (Mn–OH) react with LiPF₆ by a cation exchange reaction and HF molecules are formed according to a series of reactions¹⁹.



H^+ ions in HF produce MnO and MnO_2 according to $2LiMn_2O_4 + 4H^+ \rightarrow 3MnO_2 + MnO + Li_2O + 2H_2O$ ²⁰. Also the Mn dissolution can be chemically occurred by HF attack²¹. Formation of MnO_2 and MnF_2 occurs according to the following reaction on the surface of cathode and anode electrode^{22 21}.



At elevated temperature, PF_6^- ions are likely to reduce to PF_5^- , and therefore Mn^{4+} ions are more likely to reduce to Mn^{3+} , as follows²³:



This is the reason why Mn dissolution is accelerated at high temperatures²⁰ and Mn^{2+} ions are triggered in the form of MnO and MnF_2 on the cathode electrode surface^{24 22}. Furthermore, Mn ions move to anode electrode and are deposited on the anode surface. As shown in figure 7, the irreversible Li ion loss by Mn reduction is occurred on the surface of anode electrode. Therefore Mn dissolution leads to increase the resistance of the cell as well as to raise irreversible extraction of Li ions^{16d}. Mn^{2+} ions are easily reduced on the surface of graphite electrode because the redox potential of Mn/Mn^{2+} is much higher than that of graphite²⁵. Therefore Mn dissolution generates the harmful effect to cycling performance of the spinel $LiMn_2O_4$.

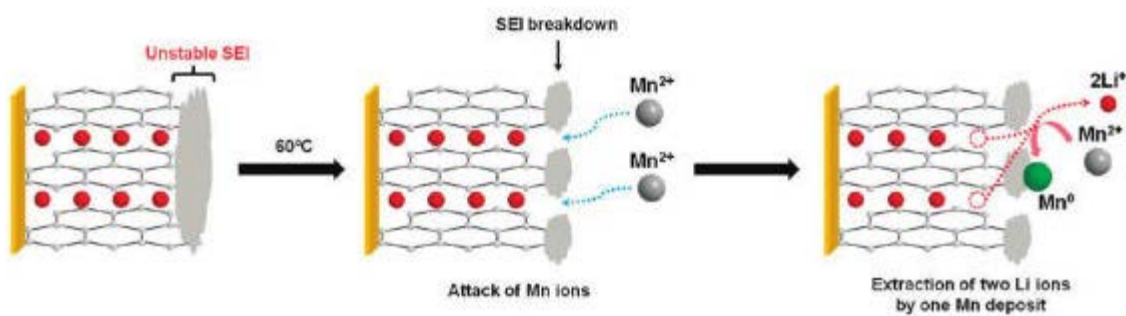


Figure 7. Schematic presentation the irreversible Li ion loss by Mn reduction at anode surface⁵.

1.2.3-2 Oxygen deficiency

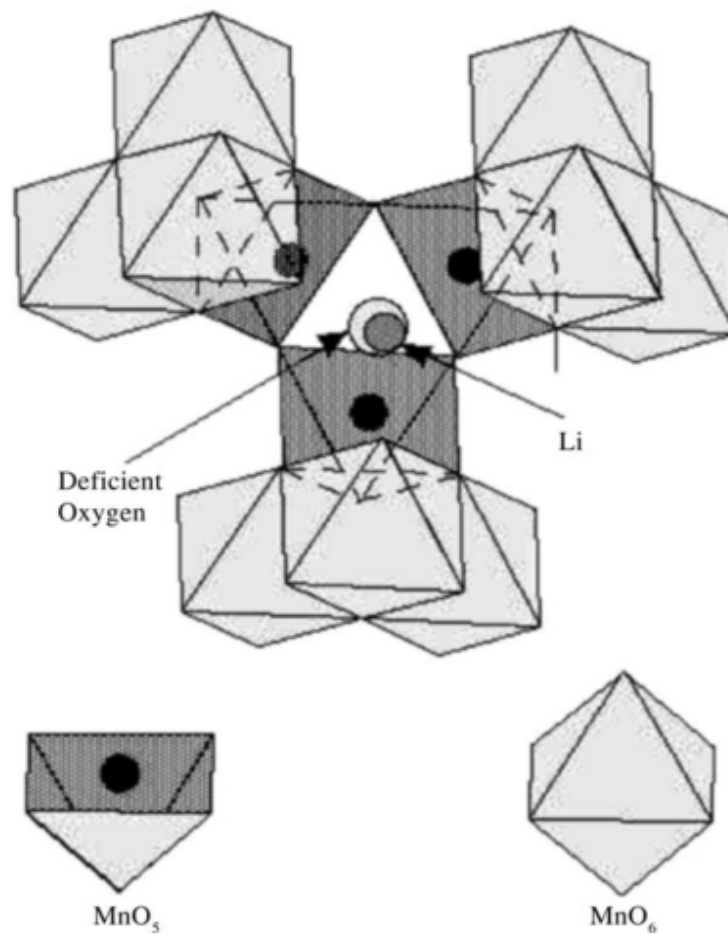


Figure 8. Structure of oxygen-deficient spinel ⁷.

Oxygen deficiency plays an important role in the stability of spinel cathode material. In the cubic spinel LiMn_2O_4 , the oxygen deficiency can be easily formed by the synthesis at high temperatures, and the charge and discharge properties are considerably affected by the oxygen deficiency in the spinel structure ²⁶.

Oxygen deficiency leads to the structure instability. This could be responsible for the capacity fading during Li^+ ion intercalation/deintercalation process at room and high temperature ^{16a}. Kanno et al. reported that the oxygen deficiency damaged the spinel structure. In this paper, it occurs that some interstitial oxygen resides in vacant 8b site with oxygen vacancy at 32e, which could lead to interrupt Li diffusion ²⁶.

As shown in figure 8, the oxygen deficient spinel is schematically described. 1mol oxygen vacancy has influence on 12mol Mn atoms. Due to three sets of MnO_5 - $(\text{MnO}_6)_3$, one oxygen defect makes three Mn ions coordinated with five oxygen (MnO_5). Oxygen deficiency contributes to electrochemical voltage profile of spinel. As shown in the figure 9, it can be observed through additional discharge plateau at 3.0V and 4.5V⁷.

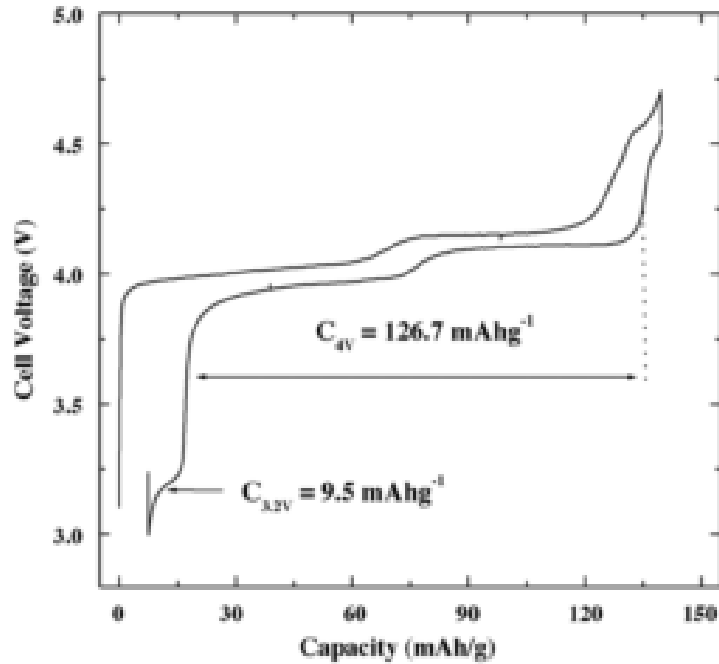


Figure 9. Charge/discharge curve of $\text{Li}_{1.002}\text{Mn}_{1.998}\text{O}_{3.981}$ ⁷.

Ikuhara et al. have revealed oxygen deficiencies in LiMn_2O_4 spinel. As shown in figure 10, the decrease in magnitude of the first peak corresponds to greater filling of the Mn 3d orbital, which indicates less oxygen in the coordination shell of Mn²⁷. The second peak of the O-K edge around 548 eV also changed. Such differences in O-K ELNES peaks are known to be related to changes in the arrangement of anions around the central Mn atoms¹³. These are the evidences of presence of oxygen vacancies. There are more oxygen vacancies at the surface than the core of LiMn_2O_4 . The Oxygen deficiency of LiMn_2O_4 spinel can be improved by metal doping or synthesizing under pressured O_2 atmosphere^{17d, 28}.

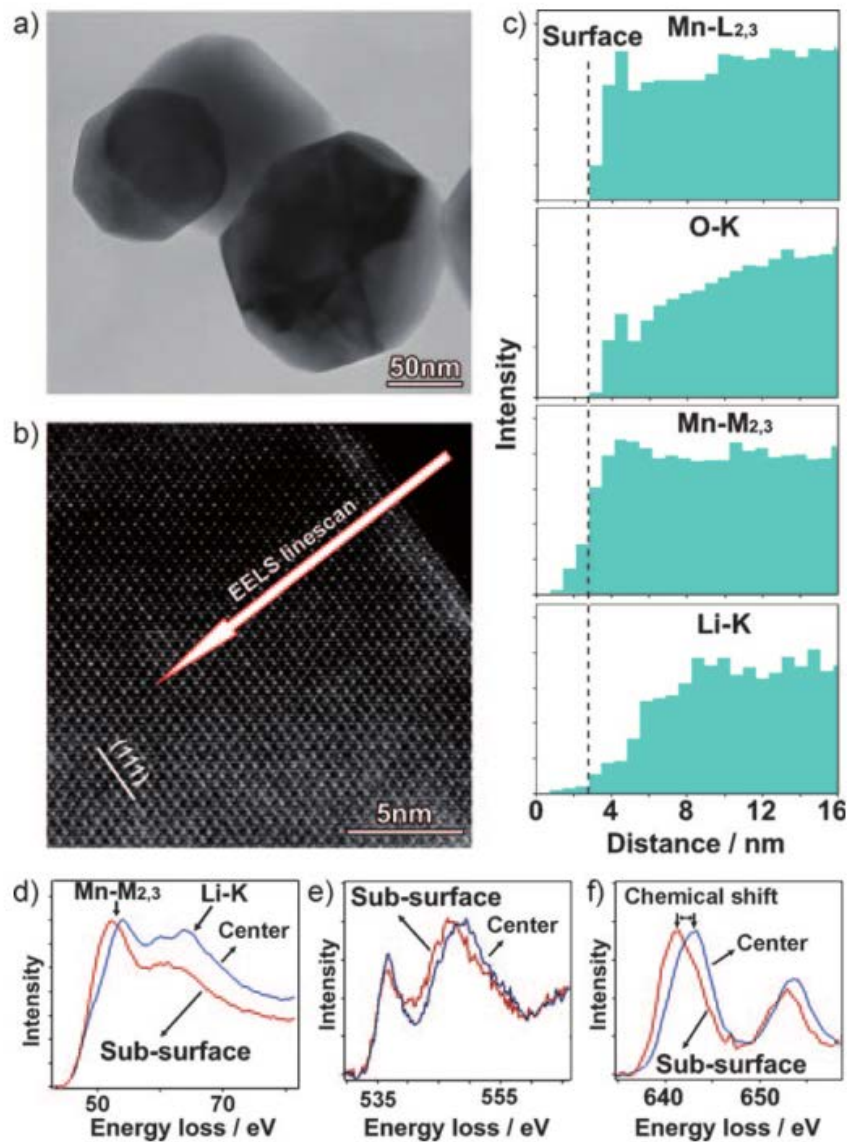


Figure 10. (a) TEM image of LiMn₂O₄ particles. (b) STEM image of the edge of a typical LiMn₂O₄ particle. The arrow indicates the region of the EELS line scan. (c) Integrated intensity of the Mn-L_{2,3}, O-K, Mn-M_{2,3} and Li-K edges. (d) ELNES of Mn-M_{2,3} and Li-K showing the difference in Li concentration between the center and surface regions, as well as the chemical shift of Mn-M_{2,3}. (e) ELNES of O-K edge showing the differences in pre-peak height and main peak position between the center and surface regions. (f) ELNES of the Mn-L_{2,3} edge showing a chemical shift from the center to the surface region¹³.

1.2.3-3 Jahn-Teller distortion



Figure 11. Upper panel: crystal-field splitting of five-fold degenerate atomic 3d levels into lower t_{2g} (triply degenerate) and higher e_g (doubly degenerate) levels. Jahn-Teller distortion of MnO_6 ¹².

More lithium ions can insert into the octahedral 16c sites of Spinel $LiMn_2O_4$. Therefore, a theoretical capacity of $LiMn_2O_4$ increased up to 300mAh/g. It shows two different voltage regions (2.8V, 4V vs. Li^+/Li^{10}) and the average oxidation state of Mn ion changes from +3.5 to +3 when the lithium sites are fully occupied ($Li_2Mn_2O_4$). However, additional lithium ions in the spinel $LiMn_2O_4$ cause a serious structural changes resulting from Jahn-Teller distortion because of the raised portion of Mn^{3+} . The d-electron configuration of the coordinated Mn^{3+} ions causes Jahn-Teller distortion in the spinel structure (Figure11) ¹². Splitting of the 3d-electron energy levels induced by jahn-Teller distortion leads to anisotropically dimensional changes. In the case of Spinel $LiMn_2O_4$, length of metal-ligand bond is extended along the c-axis by 12% and is shrunk along the a-axis by 3% resulting

in 5.6% expansion in unit cell volume¹⁰.

By these reasons, as Li ions are inserted/extracted into/from the structure of LiMn_2O_4 , crystal structure changes from the cubic spinel (space group: $Fd\bar{3}m$) to the tetragonal spinel (space group: $I4_1/amd$). These two phases coexist rather than a solid solution in figure 12 region III^{18a}. It leads to a severe capacity fading in the 3V region²⁹. Accordingly, due to the problems above, only 4V region can be available.

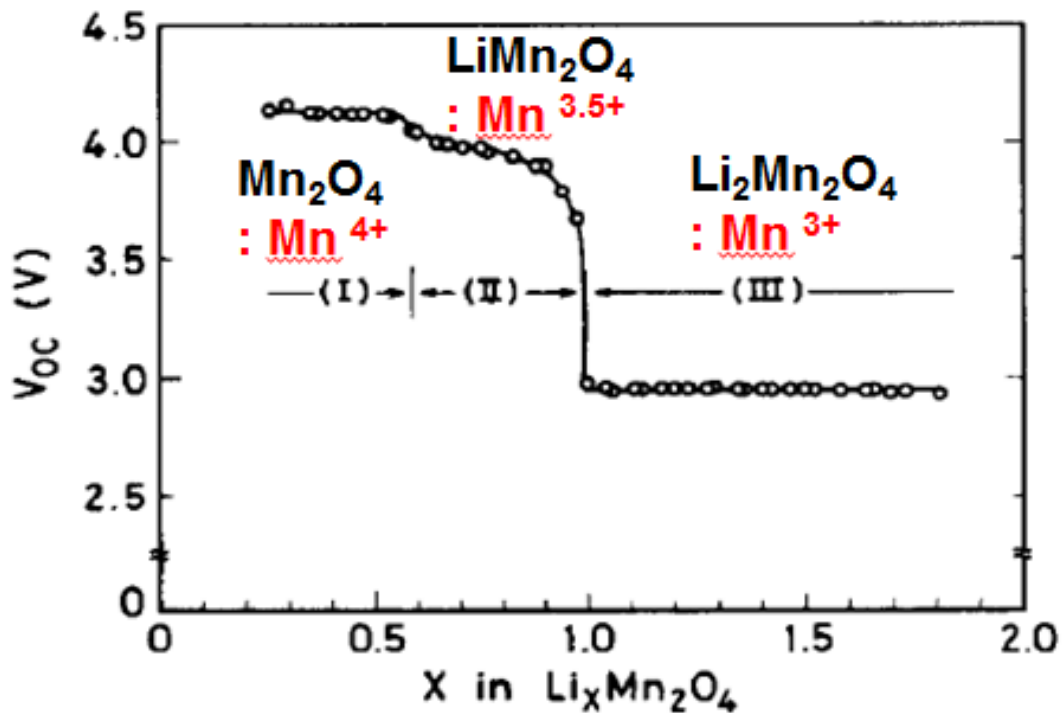


Figure 12. Open circuit voltage of $\text{Li}_x\text{Mn}_2\text{O}_4$ as a function of x ; (I) cubic LiMn_2O_4 and cubic Mn_2O_4 , (II) cubic $\text{Li}_x\text{Mn}_2\text{O}_4$ and (III) tetragonal $\text{Li}_2\text{Mn}_2\text{O}_4$ and cubic LiMn_2O_4 ¹⁰.

1.2.4 Strategies to improve the cycling performance

Cycling performance is very important characteristic for batteries. The cycle life of the cells was affected by the structural stability as well as the stability of electrode-electrolyte interfaces. Especially, cycling performance at elevated temperature is crucial because most of cathode materials are unstable at elevated temperature because the formations of HF and side reaction on the surface are accelerated. Thus, the significant capacity fading is observed during cycling. There are several strategies to improve the cycling retention at elevated temperature. The poor cycling retention at elevated temperature can be improved by cationic substitution, anionic substitution and surface treatment on LiMn_2O_4 .

In case of the cation substitution, cations (Li, Co, Mn, Ni, Al, Zn, etc.) are occupied into Mn 16d sites, and the valence state of Mn increases above 3.5. As a positive effect, Jahn-Teller distortion has decreased. Consequently, tetragonal phase transition (Jahn-Teller distortion) is suppressed because the amount of Mn^{3+} decreases. Also, the amount of dissolved Mn^{2+} produced by disproportionation reaction is reduced. As shown in figure 13, there is remarkable progress in the cycle performance of $\text{LiM}_x\text{Mn}_{2-x}\text{O}_4$ (M=Li, Co, Mn, Ni, Al and Zn etc).

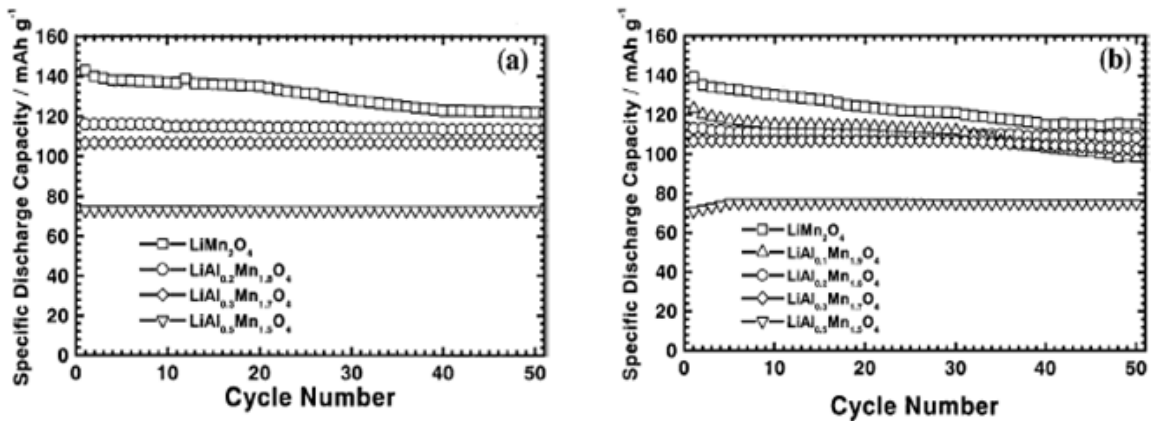


Figure 13. Specific discharge capacities vs. cycle number of $\text{LiAl}_x\text{Mn}_{2-x}\text{O}_4$ electrodes cycled between 3.4 and 4.3 $V_{\text{Li/Li}^+}$ (a) 25 and (b) 45°C⁸.

However, cationic substitution also has a problem of decreasing a capacity with increasing dopant content because the capacity is proportional to the amount of Mn^{3+} ³⁰.

For these reasons, researchers have studied anionic substitution in oxygen 32e sites. Jiang et al. reported that the initial discharge capacity of $\text{Li}_{1.05}\text{Mn}_{1.95}\text{O}_{3.95}\text{F}_{0.05}$ was increased to 128 mAh g^{-1} , and the capacity degradation during cycling was suppressed by the co-doping of Li and F^{31} . Further the doping in spinel LiMn_2O_4 with Cl improved cycling performance due to stronger Mn-Cl bonds than Mn-O bonds³². However, with increasing dopant content anionic substitution also has a disadvantage due to increased Jahn-Teller active Mn^{3+} . During cycling at elevated temperatures, the side reactions on the surface such as Mn dissolution and the electrolyte decomposition occurred more significantly³³. Thus, the amount of dopant ions should be small to reduce disadvantages of doping strategies.

As another solution to hinder Mn dissolution at elevated temperature, the surface coating is intensively studied of the metal oxides such as Al_2O_3 ³⁴, AlPO_4 ³⁵, SiO_2 ³⁶, FeO_3 ³⁷, ZnO ³⁸ and MgO ³⁹ etc. have been used to suppress the Mn dissolution and undesirable side reactions. The coating layer protects the surface of LiMn_2O_4 from being directly exposed to the highly active electrolyte. However, the thick coating layer acts as a resistive layer which interrupt the Li ion diffusion and electron conduction because it is electrochemically inactive metal compounds^{34a}. The electrochemically active lithium metal oxides can be a coating material such as LiCoO_2 ^{40 41 42}, $\text{LiNi}_{0.5}\text{Mn}_{0.5}\text{O}_2$ ^{43 44 45}, and $\text{LiNi}_{0.8}\text{Co}_{0.2}\text{O}_2$ ⁴⁶. As these materials are more stable in the electrolyte than LiMn_2O_4 , the coating layer prevented the direct contact between LiMn_2O_4 and electrolyte⁴². As a result, the electrode materials are better candidate for coating materials (figure 14). However, it should be considered that the oxygen array of host material should be the same to that of coating material to reduce interfacial resistance.

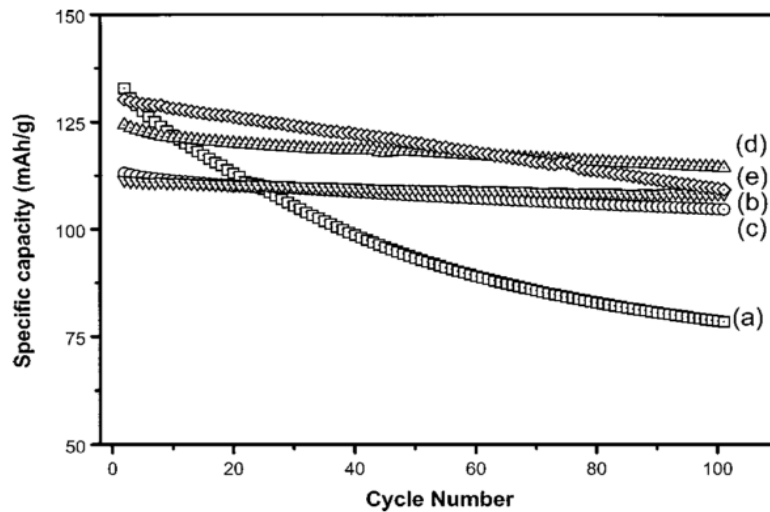


Figure 14. Cycling performance data of (a) LiMn_2O_4 , (b) $\text{LiCo}_{0.5}\text{Ni}_{0.5}\text{O}_2$ -modified LiMn_2O_4 , (c) LiCoO_2 -modified LiMn_2O_4 , (d) $\text{Li}_{0.75}\text{CoO}_2$ -modified LiMn_2O_4 , and (e) Al_2O_3 -modified LiMn_2O_4 at a current density of $0.5\text{mA}/\text{cm}^2$ (C/2 rate) at 60°C ⁹.

Recently, our group reported the research results to improve cycling retention of spinel material with high capacity (>120 mAh/g) at elevated temperature. The epitaxial relationship between layered material ($R\bar{3}m$) and spinel material ($Fd\bar{3}m$) prevented from increasing the interfacial resistance. This epitaxially grown layered surface enhanced the cycle life retention and thermal stability at the elevated temperature (60°C)⁴⁷. And by double coating of highly doped spinel on LiMn_2O_4 , the formation of hierarchical structures; Cubic spinel, tetragonal spinel, and monoclinic layered LiMnO_2 was made on the surface. The changes in the surface microstructure can reduce the activation barrier for lithium-ion diffusion⁴⁸. Then our group researched about the surface Mn oxidation state, which is controlled by coated with cobalt-substituted spinel⁴⁹. By controlling the oxidation state of active transition metal ions, the electronic conductivity and lithium diffusion coefficient are improved. It leads to high rate capability and cycling retention at 60°C . However these above materials are insufficient for the batteries for EVs.

Therefore in this paper, we tried to develop high capacity and high thermal stability spinel material for EVs. We made Al doped spinel as bare and then optimize it for best cycling performance at elevated temperature. And then we proceed with coating and doping simultaneously. The coating layer can protect the surface of bare from directly exposing to the HF in electrolyte and suppress the dissolution of Mn ions. Fluorine is doped into vacant oxygen site. So fluorine doping had the effect of elevating the specific capacity and stabilizing the structure of the spinel⁵⁰. Accordingly, the cycle performance especially at elevated temperature is improved. This coated LiMn_2O_4 showed a discharge capacity of 120.1mAh g^{-1} . And it exhibited a discharge capacity retention of 94.0% at high temperature at 60°C after 100cycles. From these results, this new coated spinel cathode material had high capacity and excellent thermal stability.

II. Experiment

2.1 Experimental method

Bare $\text{Li}_{1.015}\text{Al}_{0.06}\text{Mn}_{1.925}\text{O}_4$ was synthesized via typical solid-state reaction. Stoichiometric amounts of Mn_3O_4 , $\text{Al}(\text{NO}_3)_3$ and Li_2CO_3 were dissolved in distilled water and heated at 120°C until dried, then it was mixed and annealed at 650°C for 5hr and 800°C for 17hr under oxygen atmosphere. After calcination, it was thoroughly mixed and heated again at 750°C for 10hr under oxygen atmosphere to reduce impurity phase.

To prepare the coated sample, Bare $\text{Li}_{1.015}\text{Al}_{0.06}\text{Mn}_{1.925}\text{O}_4$ were coated with coating solution consisting of $\text{Li}(\text{CH}_3\text{COO})_2\text{H}_2\text{O}$, $\text{Mn}(\text{CH}_3\text{COO})_2\cdot 4\text{H}_2\text{O}$, $\text{Ni}(\text{CH}_3\text{COO})_2\cdot 4\text{H}_2\text{O}$ and NH_4F dissolved in distilled water by sol-gel method. The as-prepared BLMO was immersed into this solution with stirring at 120°C for 90min until dried. The resulting powder was stored in oven at 110°C for 2hr. This dried powders were heated at 750°C for 3hr under oxygen atmosphere. Final composition of this coated sample after firing at 750°C is $\text{Li}_{1.015}\text{Al}_{0.06}\text{Mn}_{1.925}\text{O}_{3.98}\text{F}_{0.02}$ and coating amount was 2.25wt% of the bare sample weight.

2.2 Electrochemical measurement

The cathode electrodes were consisted of 90 wt% prepared powders, 5wt% Super P carbon black, and 5wt% polyvinylidene fluoride (PVDF) binder. The mixed slurry was coated on Al foil and dried in oven at 120°C for 2hr. And then the electrode was pressed. The electrochemical test were carried out using CR2032 coin-type cell, which contains a cathode electrode and a lithium metal anode separated by the porous polypropylen. These were assembled in a dry argon-filled glove box. The electrolyte was 1.1 M LiPF_6 in mixture of ethylene carbonate (EC) and diethylene carbonate (DEC) in 1:1 volume ratio (PANAX ETEC Co. Ltd., Korea). The galvanostatic charge-discharge tests were conducted in a voltage range of 4.3 to 3.0 V vs. Li/Li^+ . The active material loading density was 6 mg cm^{-2} . Before electrochemical tests, the cells were galvanostatically charged to 4.3 V at 0.1 C rate, and maintained at 4.3 V until the current decreased to 0.005C rate, then discharged to 3.0 V vs Li/Li^+ .

2.3 Instrumental analysis

Structural analysis: The crystalline phase of samples was analyzed by powder X-ray diffractometer (XRD, D/MAX-2200V, Rigaku) using Cu Ka radiation. XRD patterns of cathode electrodes which were fully discharged to 3V before and after cycling at 60°C, were analyzed to observe the structural changes of samples after cycling at 60°C. XPS was measured using an Escalab instrument (Escalab 250 xi, Thermo Scientific, England), The morphology of two samples was examined by scanning electron microscopy (SEM, S-4800, HITACHI). Transmission electron microscopy samples were prepared by focused ion beam (FIB, Quanta 3D FEG, FEI). The high resolution-transmission electron microscopy (HR-TEM, JEM-2100F, JEOL) operating at 200 kV was used for analyzing a microstructure with an atomic scale.

The electrochemical impedance spectroscopy (EIS, IVIUM) was carried out to check impedance from 0.02 to 250 kHz frequency. For the EIS analysis, the cells were charged to 4.3V at 0.1C rates. The obtained results were analyzed by using ZView software.

III. Results and discussions

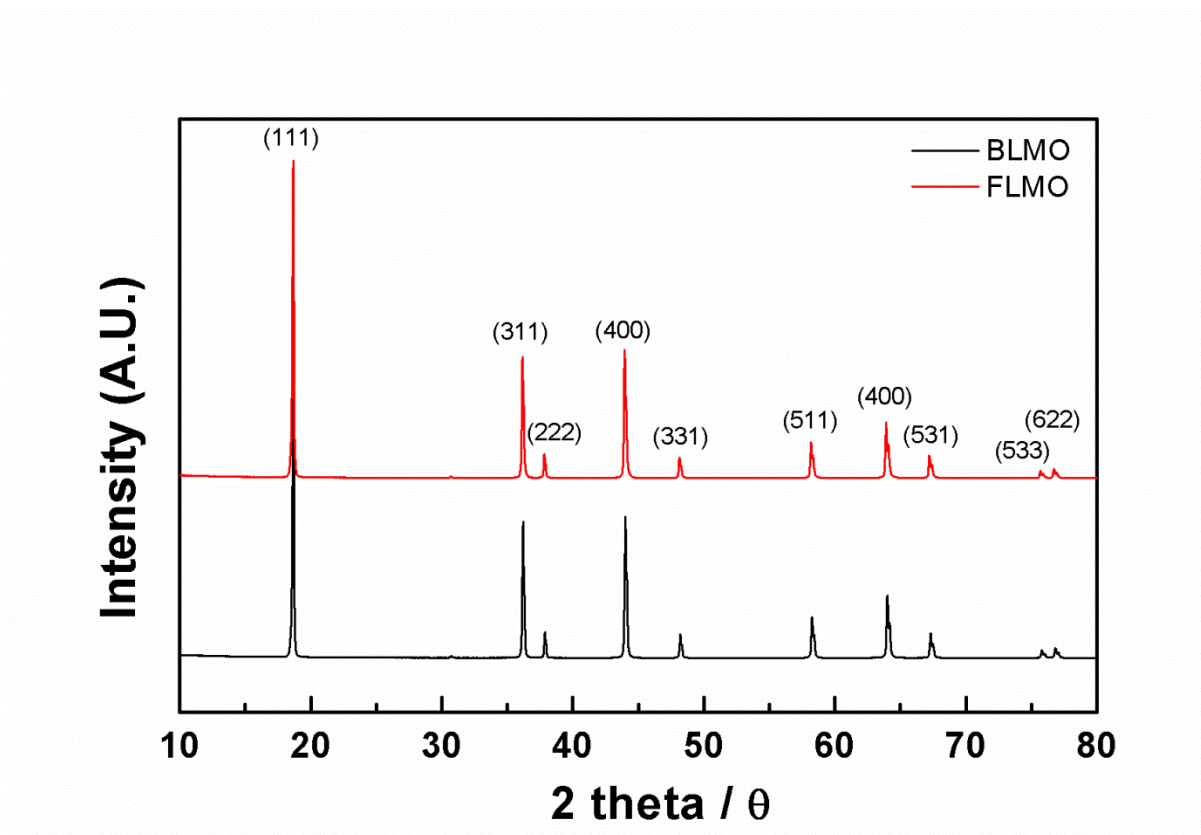


Figure 15. X-ray diffraction patterns for BLMO (black) and FLMO(red).

Table 1. Characterization of BLMO and FLMO.

Sample	Lattice parameter (\AA)	FWHM (311)
BLMO	8.2363	0.1178
FLMO	8.2210	0.1106

Figure 15 shows the XRD patterns of the bare spinel $\text{Li}_{1.01}\text{Al}_{0.06}\text{Mn}_{1.93}\text{O}_4$ (denoted as BLMO) and $\text{LiNi}_{0.5}\text{Mn}_{0.5}\text{O}_2$ coated and fluorine doped spinel $\text{Li}_{1.01}\text{Al}_{0.06}\text{Mn}_{1.93}\text{O}_{3.98}\text{F}_{0.02}$ (denoted as FLMO) powders. All peaks of samples well exhibited a single phase of cubic spinel ($Fd-3m$) without any impurities. The XRD patterns of FLMO were similar to that of BLMO. The layered phase ($R-3m$) diffraction peaks were not observed in FLMO because small amount of coating material (2.25 wt%) was contained and XRD patterns of layered phase were similar with spinel phase⁴⁷. Also fluorine-substitution for oxygen does not change the basic structure of spinel. Table 1 displays the lattice parameters and FWHM (full width at half maximum) of BLMO and FLMO. The lattice parameter of the FLMO (8.2210 Å) was smaller than BLMO (8.2363 Å) because the some portion of coating elements such as Li and Ni might diffuse into Mn sites in the host structure during heating at 750°C. Therefore, the average oxidation state of Mn increases leading to reducing lattice parameter due to smaller ionic radius of Mn^{4+} (0.53 Å) than Mn^{3+} (0.645 Å).⁵¹ Also the ionic radius of O^{2-} ion (1.40 Å) is bigger than that of F^- ion (1.33 Å). So, fluorine-substitution may lead to decreasing the lattice parameter. However, this difference doesn't have large effect on the lattice parameter because variation of Mn oxidation state by fluorine-substitution was slight.

Figure 16 displays SEM images of two samples, BLMO and FLMO. The particle sizes of BLMO and FLMO are approximately 10-15 μm and it has spherical morphologies. The morphology of the BLMO is similar to that of FLMO. The surface of BLMO is covered with by-products such as Li_2CO_3 ⁵². While, the surface morphology of FLMO is more aggregated and clean than that of BLMO. The energy dispersed X-ray (EDX) analysis is shown in figure 17. According to the EDX data, nickel and fluorine elements were evenly dispersed..

Figure 18 shows X-ray photoelectron spectroscopy (XPS) spectra of BLMO and FLMO. In case of BLMO, the oxidation state of Mn of surface is slightly different from that of core due to disadvantage of solid-state reaction. As can be seen, the amount of Mn^{4+} of FLMO on the surface was larger than that of BLMO.. This data demonstrates that the coating material ($\text{LiNi}_{0.5}^{2+}\text{Mn}_{0.5}^{4+}\text{O}_2$) was well coated on the surface of FLMO. Due to the incomplete coverage and small amount of cation doing during heat treatment, the surface oxidation state of Mn couldn't react to ideal value +4. In compared with the core of BLMO and FLMO, the average oxidation state of Mn of FLMO was less than that of BLMO due to monovalent F ions replaced with divalent O^{2-} ions in case of the FLMO.

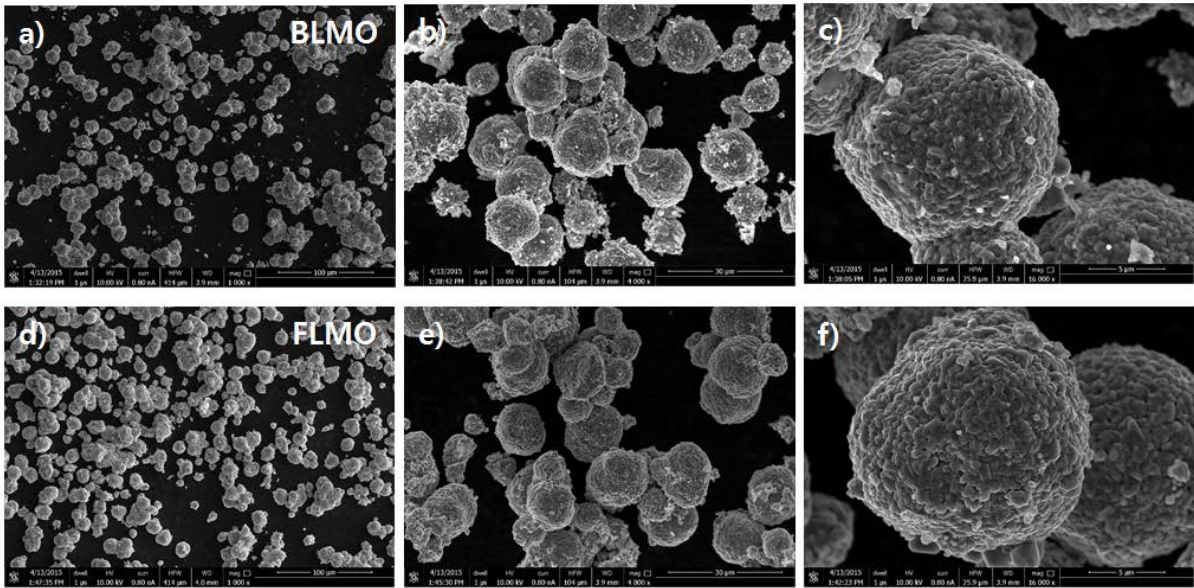


Figure 16. SEM images of BLMO (a,b,c) and FLMO (d,e,f) particles.

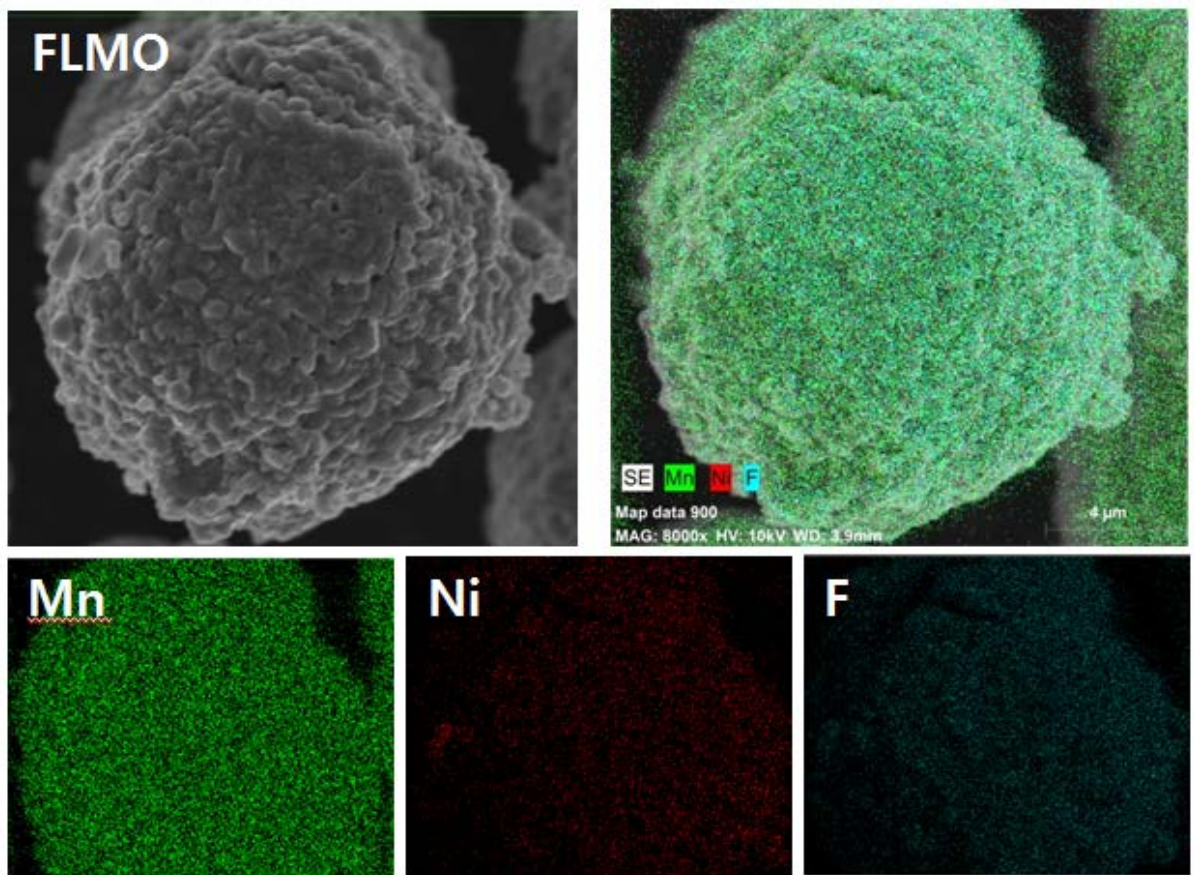


Figure 17. SEM images of FLMO and EDX mapping for Mn, Ni and Co.

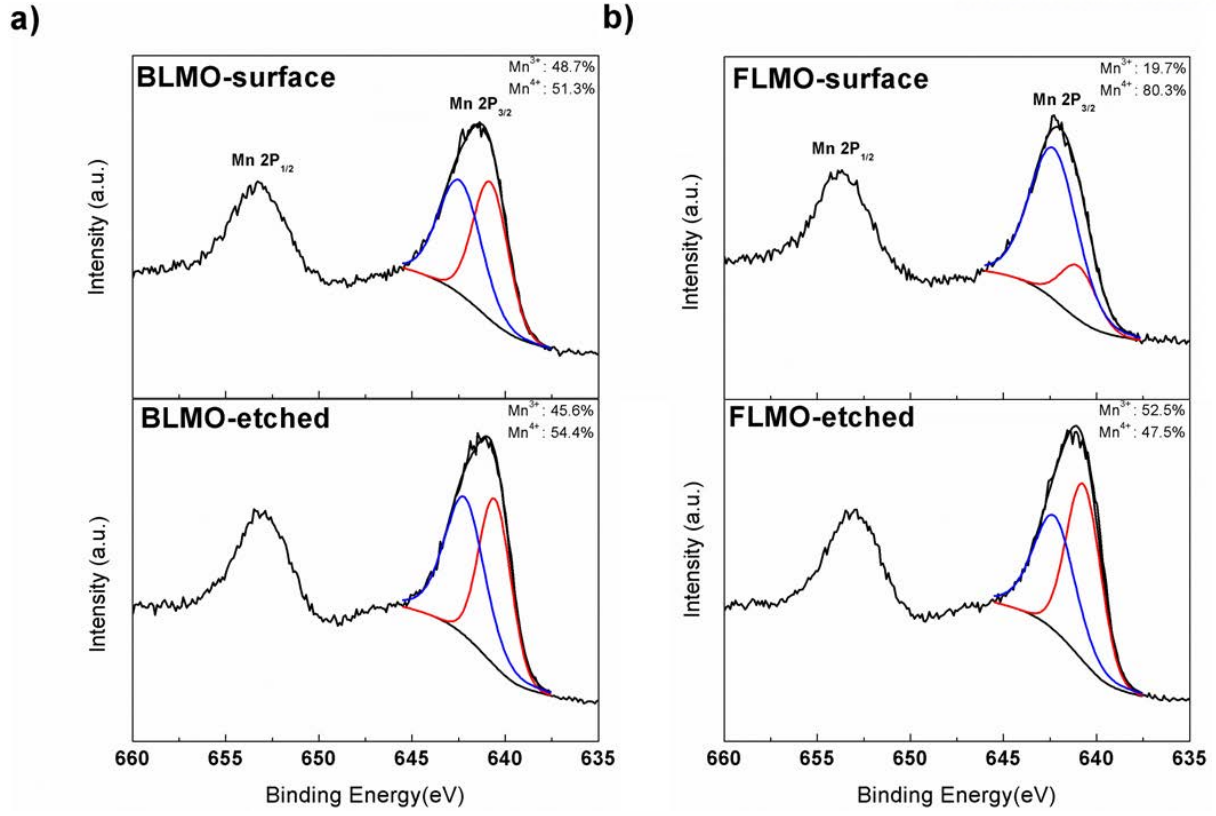


Figure 18. Mn 2p X-ray photoelectron spectroscopy (XPS) spectra of a) BLMO and b) FLMO.

To investigate microstructures with an atomic scale, the analysis of the high-resolution scanning transmission electron microscopy (STEM) was carried out. As shown in figure 19a, the STEM images of the primary particle of FLMO are exhibited. The red square areas in figure 19a are magnified on the left side. It is clearly observed that there are two different regions. The region A is spinel structure and the region B is layered structure. Two regions are connected each other without any defect. The coating material ($\text{LiMn}_{0.5}\text{Ni}_{0.5}\text{O}_2$) was epitaxially grown on the surface of the host spinel^{53, 47}. On the surface of FLMO, the layered structure was randomly observed. The spinel and layered structures are described in figure 19b and c, respectively. The both structures have cubic close packing (CCP) array of the oxygen ion. The difference can be observed by viewing the cubic [110] direction which is same as hexagonal $[\bar{2}\bar{2}1]$ viewing direction. The cubic spinel phase ($Fd\text{-}3m$) has diamond-shape (region A), when viewing direction is [110].^{16e}. There are two kinds of Mn columns. Along the cubic [110] direction, the less bright Mn columns have twice less Mn density than that of the brighter Mn columns. The region B corresponds to the layered phase ($R\text{-}3m$). The layered phase ($R\text{-}3m$) is different with cubic spinel phase. On the contrary to the spinel structure, the atoms are packed without empty site in the structure of the surface phase. It means the column consists of only invisible atom such as Li(light atom) along the viewing direction($[\bar{2}\bar{2}1]$). All octahedral sites are filled with Li or transition metal. Along the hexagonal $[\bar{2}\bar{2}1]$ direction, the transition metal atoms have same density. Therefore, along the viewing direction ($[\bar{2}\bar{2}1]$), all columns had same contrast and the atoms are packed full in the structure of the layered surface phase. It is difficult to find doped F element by STEM image because the fluorine doped into the vacant 32e oxygen site is not easily searched through this tool^{50a, 50b, 50d, 50e}. Therefore, , the EDX analysis was carried out to analyze doped F element. Figure20a exhibits TEM image of cross-sectioned FLMO particle. As can be exhibited in figure 20b, the amount of F gradually decreased from surface to core. .

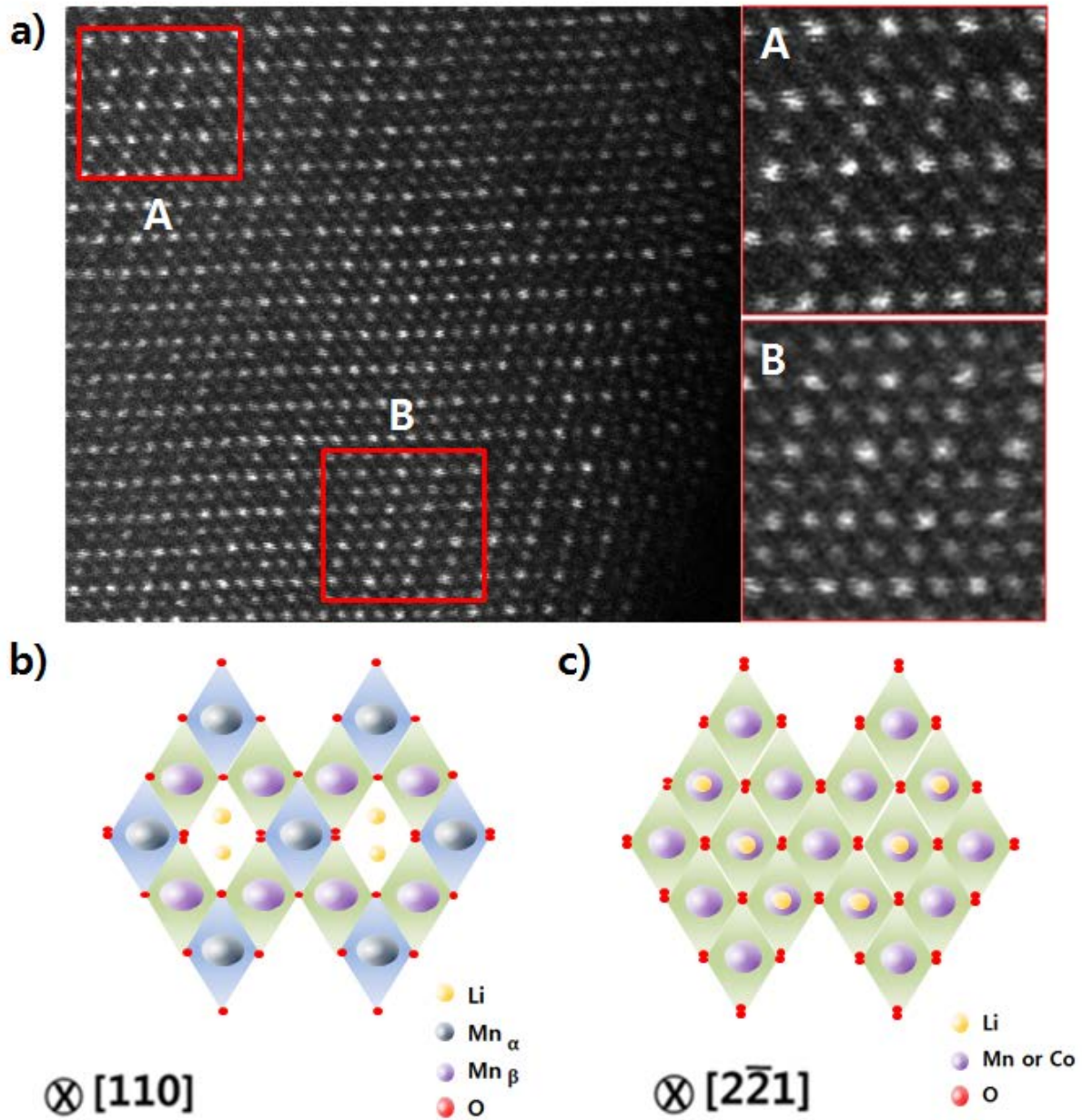


Figure 19. (a) STEM images of FLMO, (b) Structural scheme of the region A; Spinel structure viewed along the cubic $[110]$ direction (c) Structural scheme of the region B; Layered structure viewed along the hexagonal $[2\bar{2}1]$ direction.

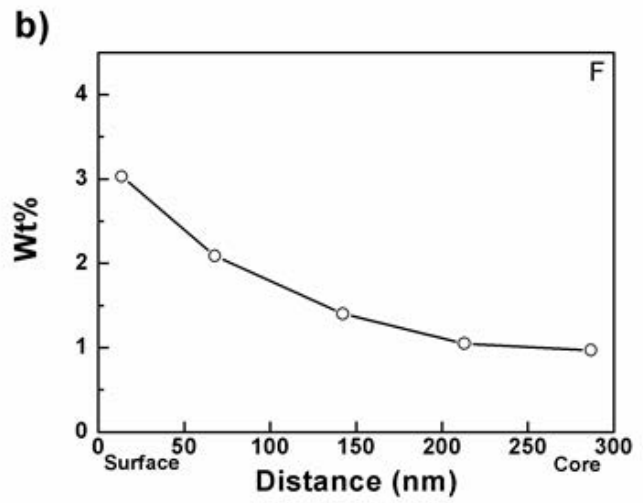
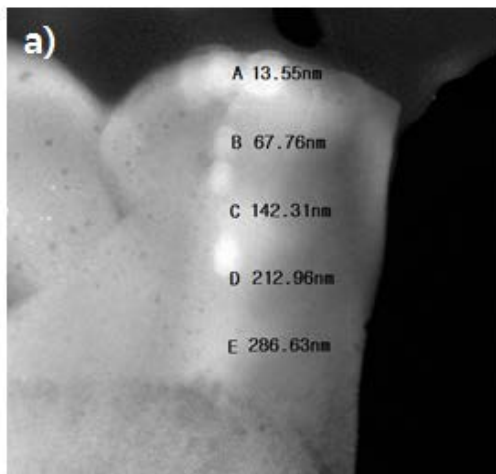


Figure 20. (a) TEM images of FLMO (b) Distribution of F element (wt%) in five pointed areas in the FLMO of figure (a).

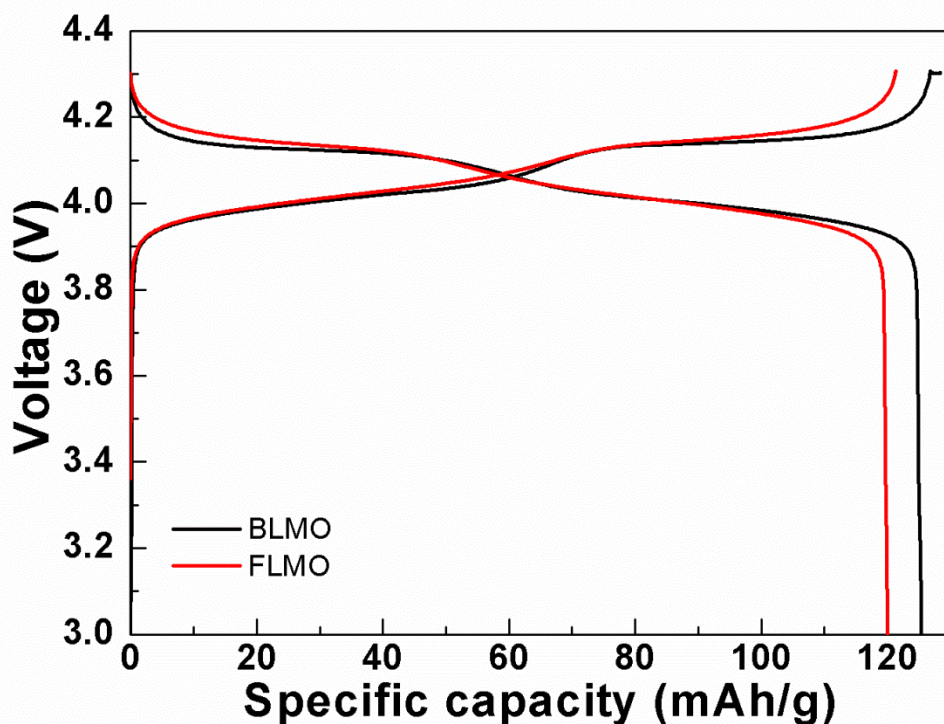


Figure 21. First charge/discharge profiles of the BLMO (black) and FLMO (red) at 0.1C rate in lithium-ion half-cells (2032R-type) at 24 °C.

The voltage profiles of BLMO and FLMO during first charge and discharge cycle are shown in figure 21. The coin type cells(2032R) were charged at 0.1C rate ($1C=120\text{mA}\cdot\text{g}^{-1}$) to 4.3V and maintained at 4.3V until the current decreased to 0.005C rates, then discharged at 0.1C rate ($1C=120\text{mA}\cdot\text{g}^{-1}$) to 3.0V at 24 °C. The discharge capacity of BLMO and FLMO were 125.4 and 120.1 $\text{mAh}\cdot\text{g}^{-1}$ and the coulombic efficiency of BLMO and FLMO were 97.7% and 98.9% respectively. The discharge capacity of FLMO was lower than that of BLMO because small amount of coated elements such as Li and Ni diffused into the host spinel⁴⁷. Also the capacity of FLMO from constant voltage mode was much lower than that of BLMO. The capacity from constant voltage mode is correlated with the overpotential. It means the FLMO electrode has lower overpotential than BLMO electrode.

Figure 22 exhibits discharge a) and charge rate b) capabilities of BLMO and FLMO at 0.5C, 1C, 3C, 5C, 7C, 10C rates during cycling in half cell. Either discharge or charge rate was fixed at 0.5 C rate at 24 °C. The discharge and charge voltage profiles of BLMO and FLMO at each C-rate were shown in figure 23. The both charge and discharge rate capacity retention of FLMO was higher than that of BLMO. For instance, the discharge capacity retention of FLMO was 85.6% (98.8mAhg⁻¹) at 10C rate of its discharge capacity at 1C rate, whereas, that of BLMO was 74.7% (89.9mAhg⁻¹). The charge capacity retention of FLMO was 70.7% (81.7mAhg⁻¹) at 10C rate of its discharge capacity at 1C rate, whereas, that of BLMO was only 58.3% (69.8mAhg⁻¹). Figure24 exhibits the discharge voltage profiles of BLMO and FLMO with decreasing temperature (25°C, 10°C, 0°C, -10°C, -20°C) at 0.1 C. The capacity retentionof FLMO was higher than that of BLMO. The BLMO and FLMO retained 87% and 92% at -10 °C, 80% and 89% at -20 °C of its initial discharge capacity, respectively. From these results, the FLMO showed improved kinetic properties because of epitaxial surface coating layer and fluorine-substitution.

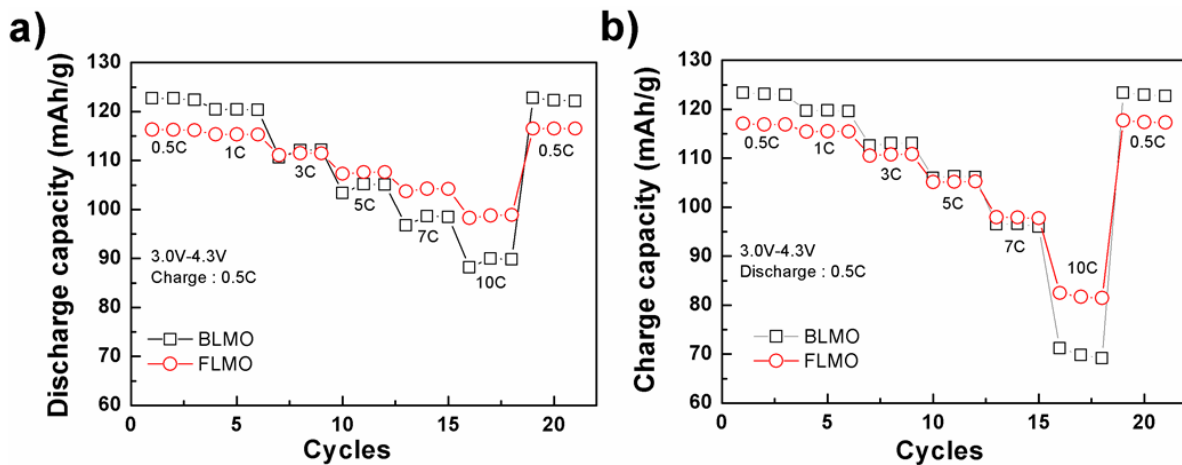


Figure 22. Electrochemical characteristics of the BLMO(black) and FLMO(red) at 24°C; (a) discharge rate capability tested between 3.0V-4.3V at 0.5C charge rate and with an increasing discharge C-rate to 10C. (b)charge rate capability tested between 3.0V-4.3V at 0.5C discharge rate and with an increasing charge C-rate to 10C.

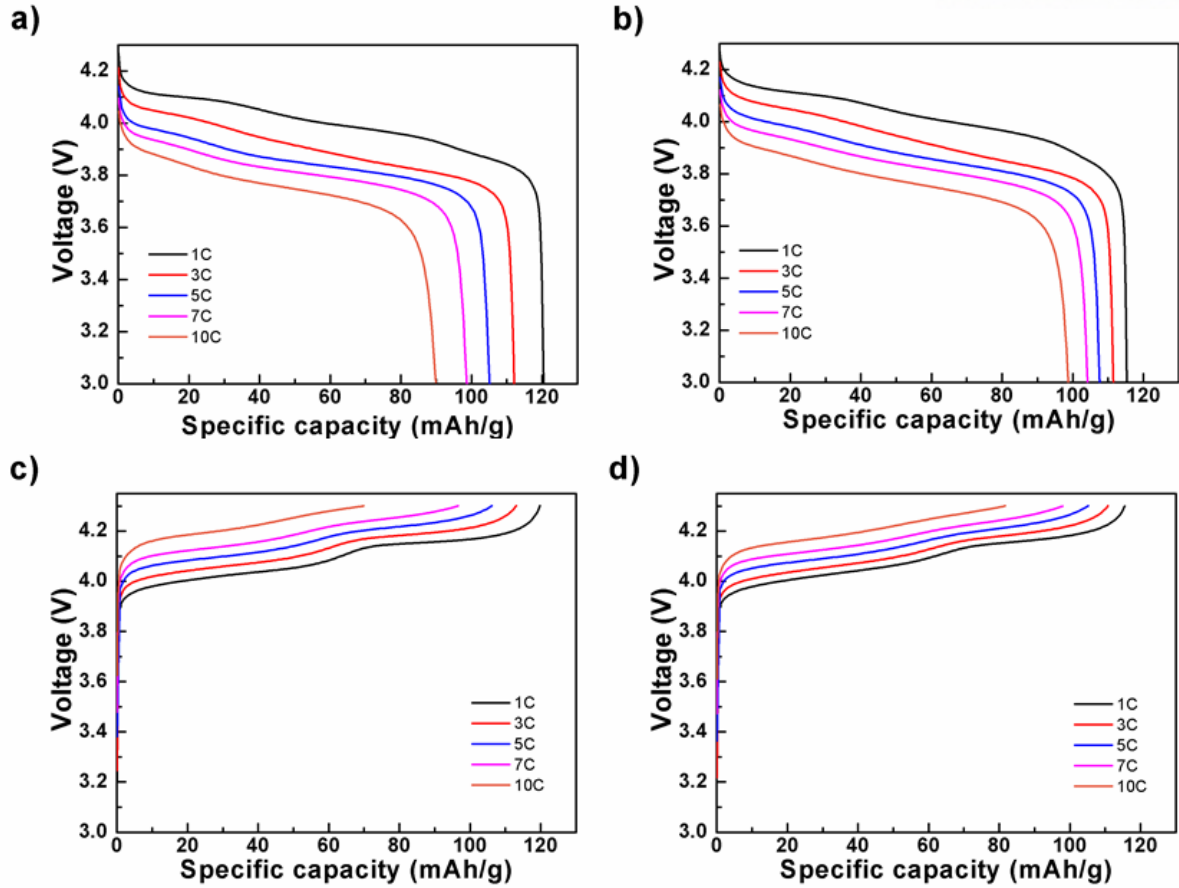


Figure 23. Initial discharge voltage profiles of the (a)BLMO and (b)FLMO materials at rates of 1, 3, 5, 7 and 10C, initial charge voltage profiles of the (c)BLMO and(d)FLMO materials at rates of 1, 3, 5, 7 and 10C.

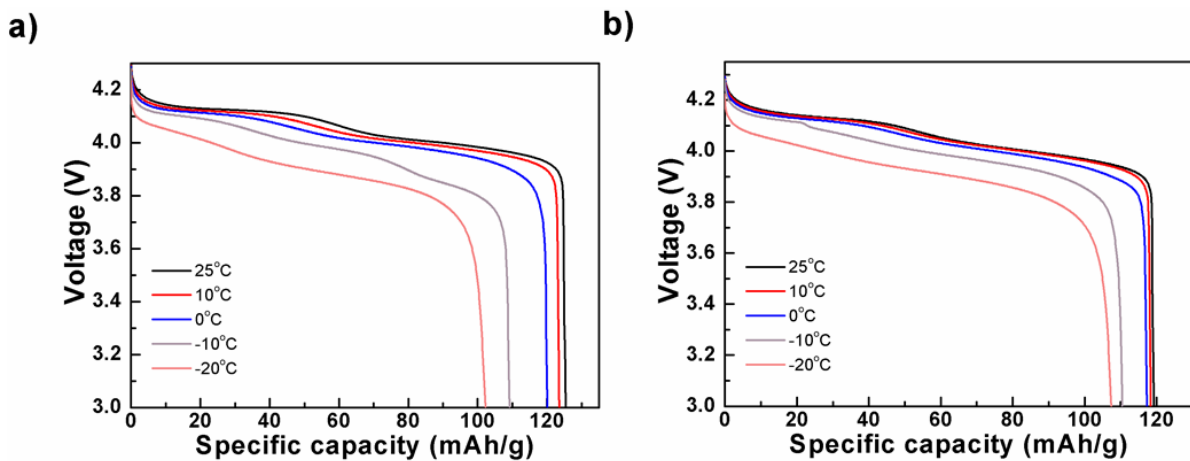


Figure 24. Discharge profiles of (a) BLMO and (b) FLMO as a function of temperatures at 0.1 C rates.

In order to find out the reasons why the FLMO had better rate capability and low temperature performance than the BLMO, we carried out an electrochemical impedance spectroscopy (EIS) shown in figure 25. Before EIS analysis, the cells were charged to 4.3V at 0.1C rates. Figure 25a shows the equivalent circuit. The impedance pattern related to electronic resistance (R_e), SEI resistance (R_{surface}), charge transfer resistance (R_{ct}) and Warburg impedance. Figure 25b exhibits the Nyquist plots of two samples after 1st and fully charged. There is no distinguishable difference between two samples. This means that epitaxially grown coating layers on the surface of spinel particles don't act as interphase resistance. We calculated the values of lithium diffusion coefficient by electrochemical impedance spectroscopy (EIS) analysis in table 2⁵⁴. The lithium diffusion coefficient could be obtained from Warburg impedance in low frequency region⁵⁵. The diffusion coefficient of FLMO was higher than that of BLMO. Lithium diffusion might be promoted due to the coated material on the surface and dopant ion in the spinel material also, on the surface, the side reactions were decreased owing to the stable surface of the FLMO. The surface phase of FLMO is epitaxially connected to the host material without any defect, which provides the efficient path for lithium ion diffusion. Based on these results, the rate capability is improved as the value of lithium diffusivity increased.

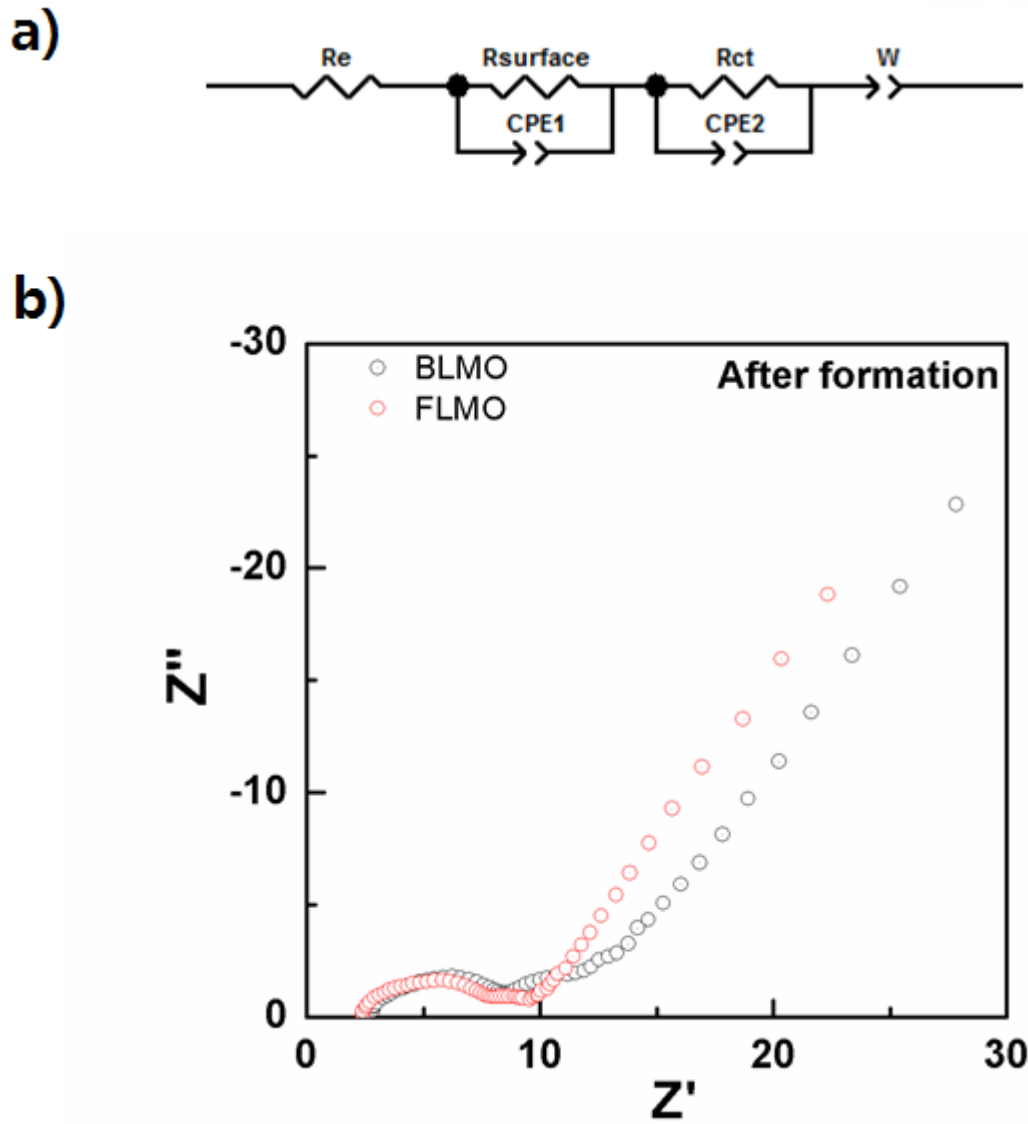


Figure 25. (a) The proposed equivalent circuit used for analyzing the impedance patterns. Nyquist plot for (b)BLMO and FLMO in regard to after formation.

Table 2. The diffusivity of BLMO and FLMO.

Sample	Diffusivity ($10^{-11} \text{cm}^2/\text{s}$)
BLMO	3.78
FLMO	7.78

The cycling performances at 60°C of the BLMO and FLMO are shown in figure 26. All cells were charged at 0.5C rates and discharged at 1C rates from 3.0V to 4.3V at 60°C. The FLMO exhibited better cycle retention of 94.0% than that of the BLMO (82.2%) after 100cycles at 60°C. The FLMO also retained 90.0% and 86.1% of its initial discharge capacity at 60°C after 200 and 300cycles. The difference of retention between bare and coated electrode is lower compared to our previous work⁴⁷, because, in this study, we optimized bare spinel material as exhibited in figure 27. The discharge retention of stoichiometric LiMn_2O_4 , $\text{Li}_{1.02}\text{Mn}_{1.98}\text{O}_4$, $\text{Li}_{1.01}\text{Al}_{0.03}\text{Mn}_{1.96}\text{O}_4$ and $\text{Li}_{1.01}\text{Al}_{0.06}\text{Mn}_{1.93}\text{O}_4$ (denoted as BLMO) was 55.5%, 71.1%, 79.0% and 82.2% after 100cycles at 60°C. The cycling performances of the BLMO, FLMO and coated sample without F doping like previous work at 60°C were displayed in figure 28. The capacity and cycle retention were increased slightly by small amount of F doping^{50a}. As shown in figure 29, less Mn was dissolved in case of FLMO. The electrode disassembled after formation cycle and charged at 0.1C rate to 4.3V. These disassembled electrodes are stored at 60°C for 2, 4 and 6 weeks. The amount of Mn dissolved in electrolyte is analyzed by ICP analysis. As a result, the loss of active materials was greatly suppressed by the surface coating and doping of fluorine. The coating phase on the surface of the FLMO can protect the host spinel by preventing the host spinel from being directly exposed to electrolyte at elevated temperature and fluorine-substitution for oxygen can suppress Mn dissolution due to strong Mn-F bond than Mn-O bond^{50a}. The electron affinity of F(328kJmol⁻¹) is greater than that of O(141kJmol⁻¹)³². Consequently the FLMO had improved cycling performances at elevated temperature and better thermal stability. The long term storage performance is exhibited in figure 30. The discharge capacity retention of BLMO and FLMO was 98.0% and 99.4% respectively. This obtained after 2 weeks stored under 60°C, with cells in fully charged state of 4.3V. The discharge capacity loss of FLMO was only 0.6% after stored at 60°C for 2 weeks, while BLMO exhibited lower capacity retention than FLMO because BLMO is unstable at elevated temperature due to manganese dissolution and oxygen deficiency.

Figure 31 shows typical Nyquist plots of the BLMO and FLMO after formation, 50th and 100th cycles. The cells are cycled at 60°C and then tested at 25°C. It was very difficult to distinguish each resistance values of the surface film (R_{sf}) and charge-transfer resistance (R_{ct}). Therefore, we compared the total impedance of the BLMO and FLMO. The total impedance of BLMO was increased more than that of FLMO with increasing cycle numbers. Nyquist plots after every 50 cycles

at 60°C are related closely to cycling performance at elevated temperature. It can be certain that severe side reactions occurred on the surface of the BLMO, which leads to worse cycling performance. Generally, the increase in total resistance of cells is due to increase of surface film (SEI) upon cycling as well as structural instability⁵⁶. Formation of SEI layer is induced by Mn dissolution and it is accelerated at elevated temperature. From these results, it is exhibited that the surface coating material on the FLMO suppressed capacity fading at elevated temperature. And also fluorine doped into vacant 32e site increases the structure stability of the FLMO^{50e}.

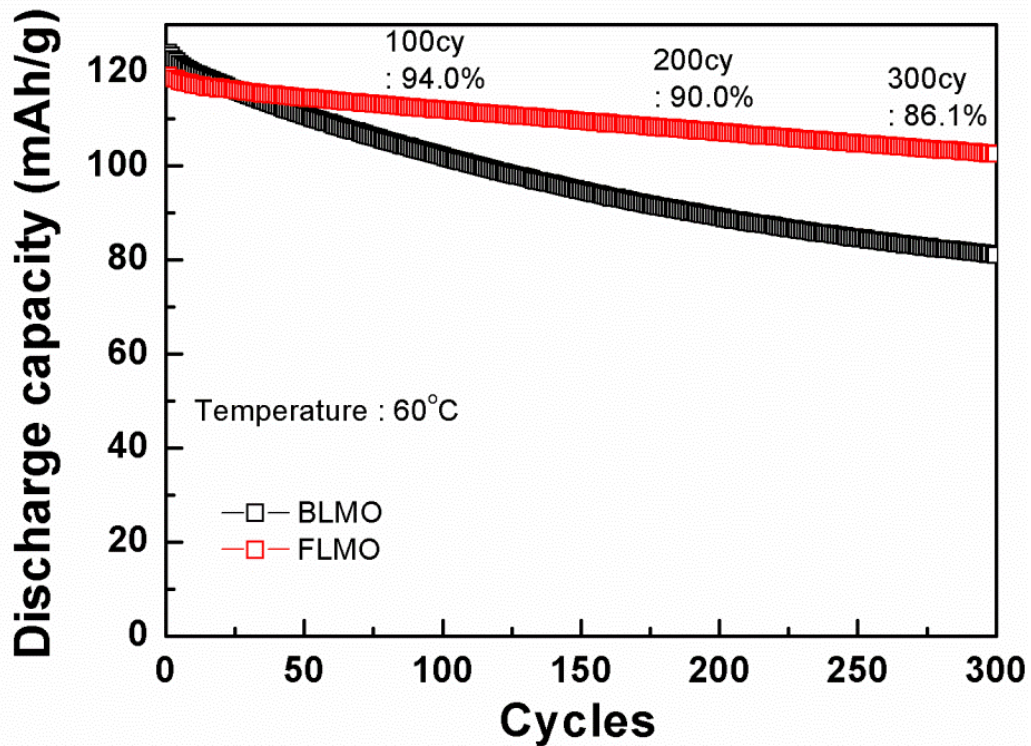


Figure 26. Cycling performances of the BLMO(black) and FLMO(red) in lithium-ion half-cells(2032R-type) at 60°C.

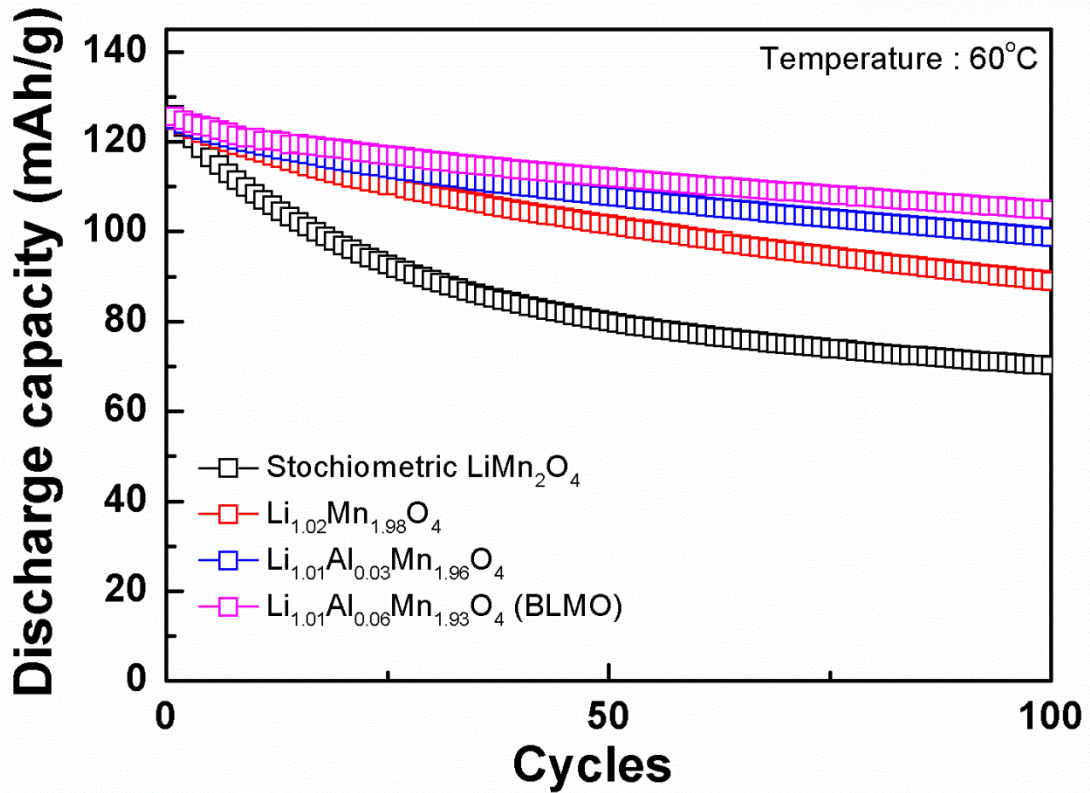


Figure 27. Cycling performances of the Stochiometric LiMn_2O_4 (black), $\text{Li}_{1.02}\text{Mn}_{1.98}\text{O}_4$ (red), $\text{Li}_{1.01}\text{Al}_{0.03}\text{Mn}_{1.96}\text{O}_4$ (blue) and $\text{Li}_{1.01}\text{Al}_{0.06}\text{Mn}_{1.93}\text{O}_4$ (magenta, denoted as BLMO)in lithium-ion half-cells(2032R-type) at 60°C.

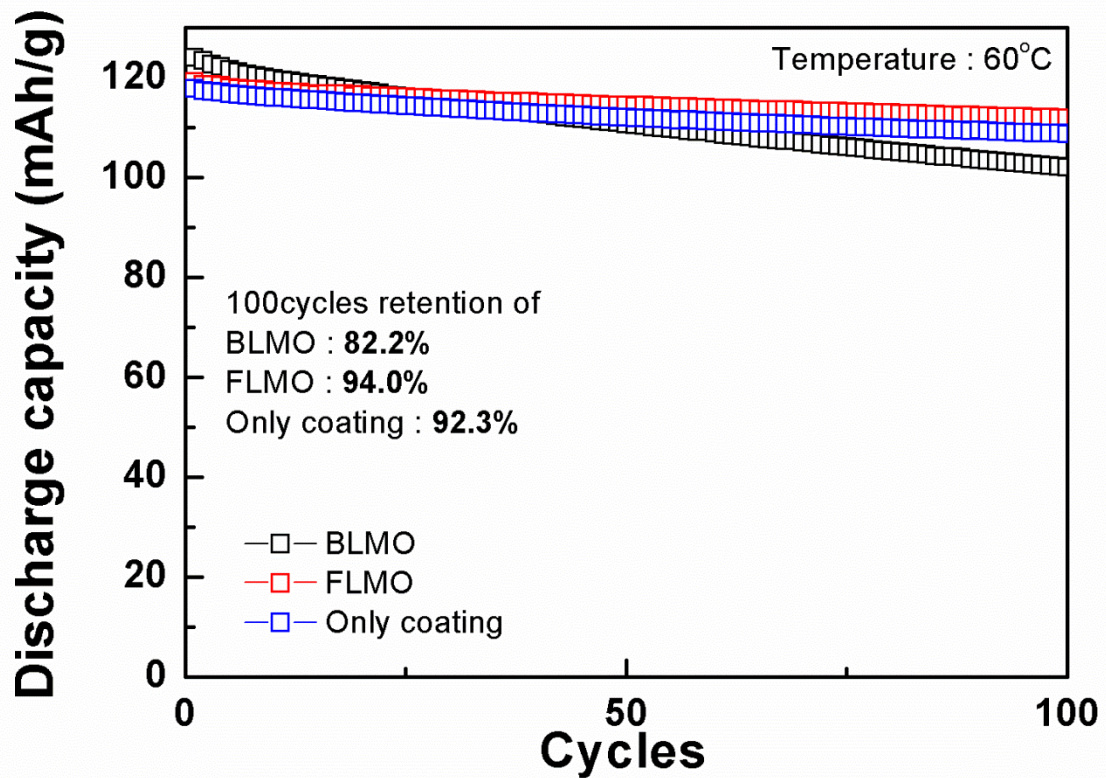


Figure 28. Cycling performances of the BLMO(black), FLMO(red) and coated sample without F doping in lithium-ion half-cells(2032R-type) at 60°C.

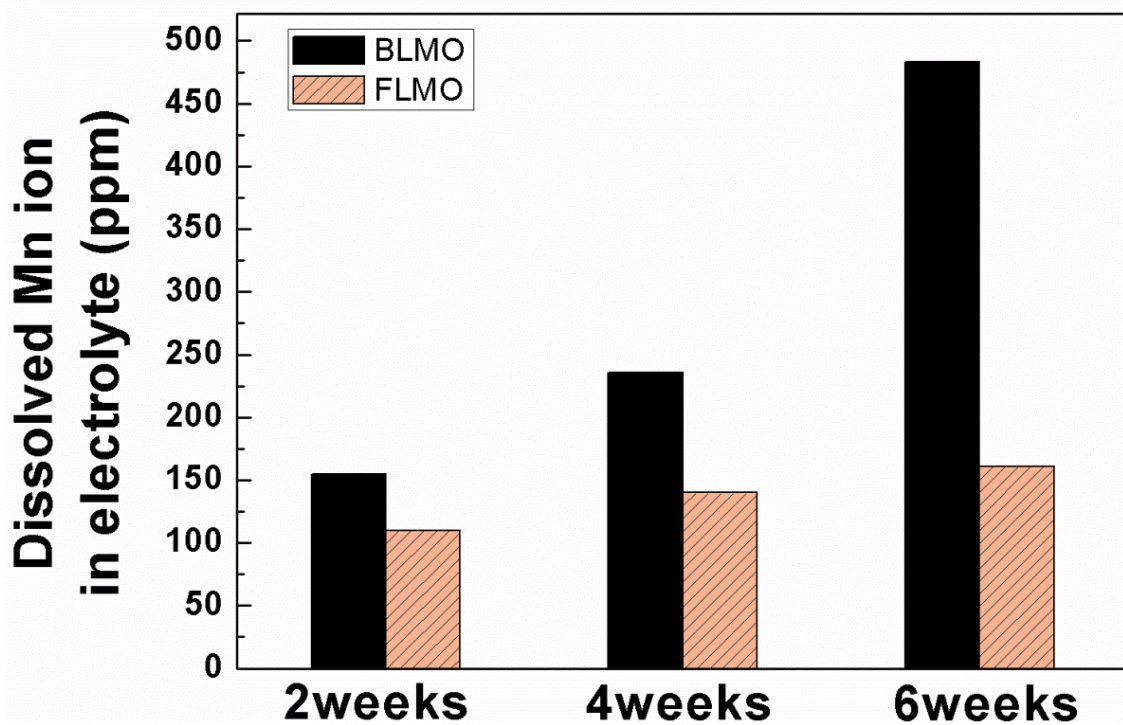


Figure 29. Mn dissolution for the electrolyte of the fully charged (to 4.3V) Li/BLMO and Li/FLMO cells during 6weeks at 60°C.

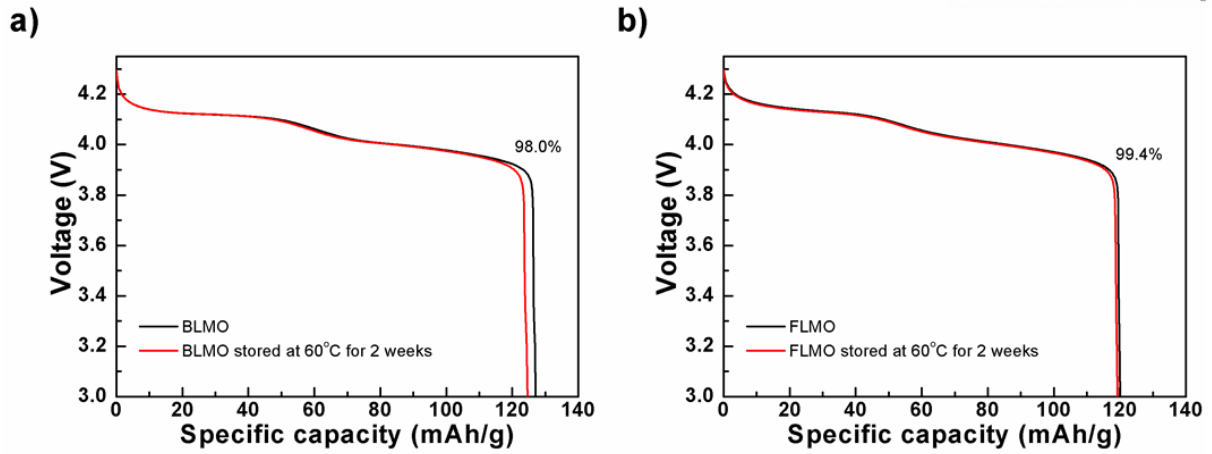


Figure 30. The discharge voltage profile of the (a) BLMO(black) and (b)FLMO(red) stored at 60°C for 2 weeks in fully-charged state of 4.3V.

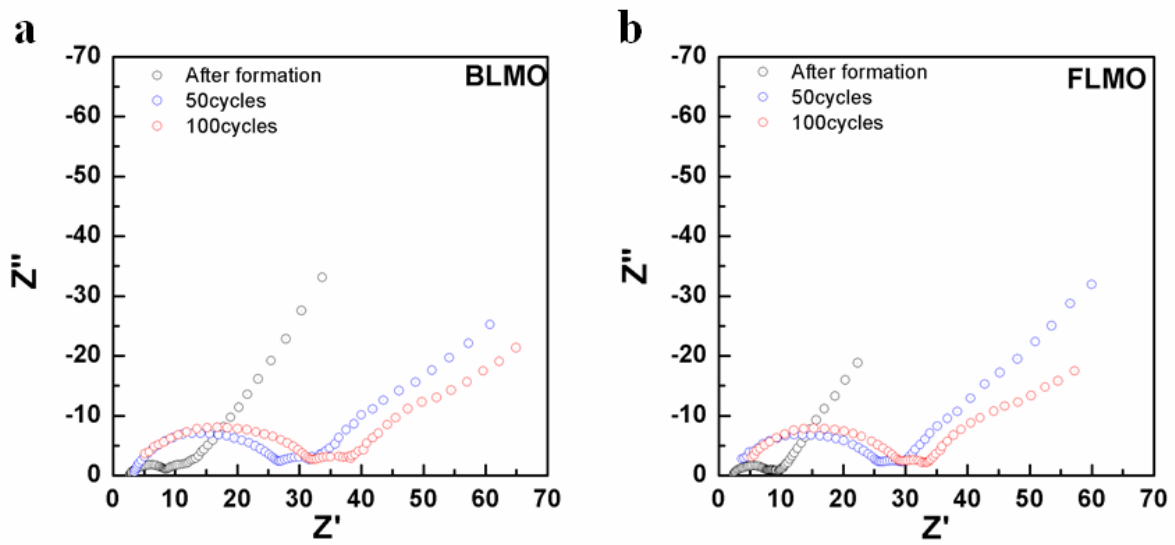


Figure 31. Nyquist plot for (a) BLMO, and (b) FLMO with respect to cycle numbers: 1st, 50th, 100th cycles.

The *Ex-situ* XRD was performed to look into structure changes of BLMO and FLMO after 100 cycles and 200cycles at 60°C. Figure 32 exhibits the *Ex-situ* XRD patterns of BLMO and FLMO; before, after 100cycles and after 200cycles at 60°C. The lattice parameter and the volume of BLMO and FLMO; before, after 100cycles and after 200cycles at 60°C were in table 3. The difference of the lattice parameter of the FLMO during cycles was very slight while that of the BLMO changed. It is reported that these phenomena are related to material loss such as manganese and oxygen during cycling⁵⁷. To evaluate structure changes, we got the difference in lattice parameter and FWHM(full width at half maximum) indicating the degree of peak broadening based on 311 diffraction line in figure 32. As shown in figure 33, FLMO exhibits less mismatch of the lattice parameter and FWHM after cycling at 60°C, while significant mismatch of the lattice parameter and FWHM can be found after cycling at 60°C. It means that the structure of the BLMO was defected and then its crystallinity may be reduced. Figure 34 shows the SEM images of BLMO and FLMO after 100cycles at 60°C. The particle of BLMO was cracked after cycling while that of FLMO had no defects. Severe side reaction produced byproduct on the surface of BLMO. The coating layer and fluorine doped into the oxygen vacant site protect host spinel against cracks on the particle. This phenomenon is associated with epitaxially grown coating layer as well as oxygen vacancies on the spinel material^{17b}.

Consequentially, the improved cycling retention of the FLMO at elevated temperature could be correlated with the layered coating layer formed on the surface of the FLMO and fluorine doped in the oxygen vacancy site of the FLMO. By acting as the protecting layer, the epitaxially grown coating layer on the surface of the FLMO leads to excellent cycle retention and thermal stability. This coating layer prevents the host spinel from being directly revealed to electrolyte and provides high oxidation state of Mn ion. The replacing Mn-O bond with Mn-F bond could also affect the chemical stability of the spinel. Fluorine substitution also leads to improving capacity retention and thermal stability because the Mn-F bonds were stronger than Mn-O bonds due to more ionic Mn-F bonds.(the electron affinity of F(328kJmol⁻¹) and O(141kJmol⁻¹)) It leads to suppression of Mn dissolution^{50a}. Therefore thermal stability and structural stability are improved.

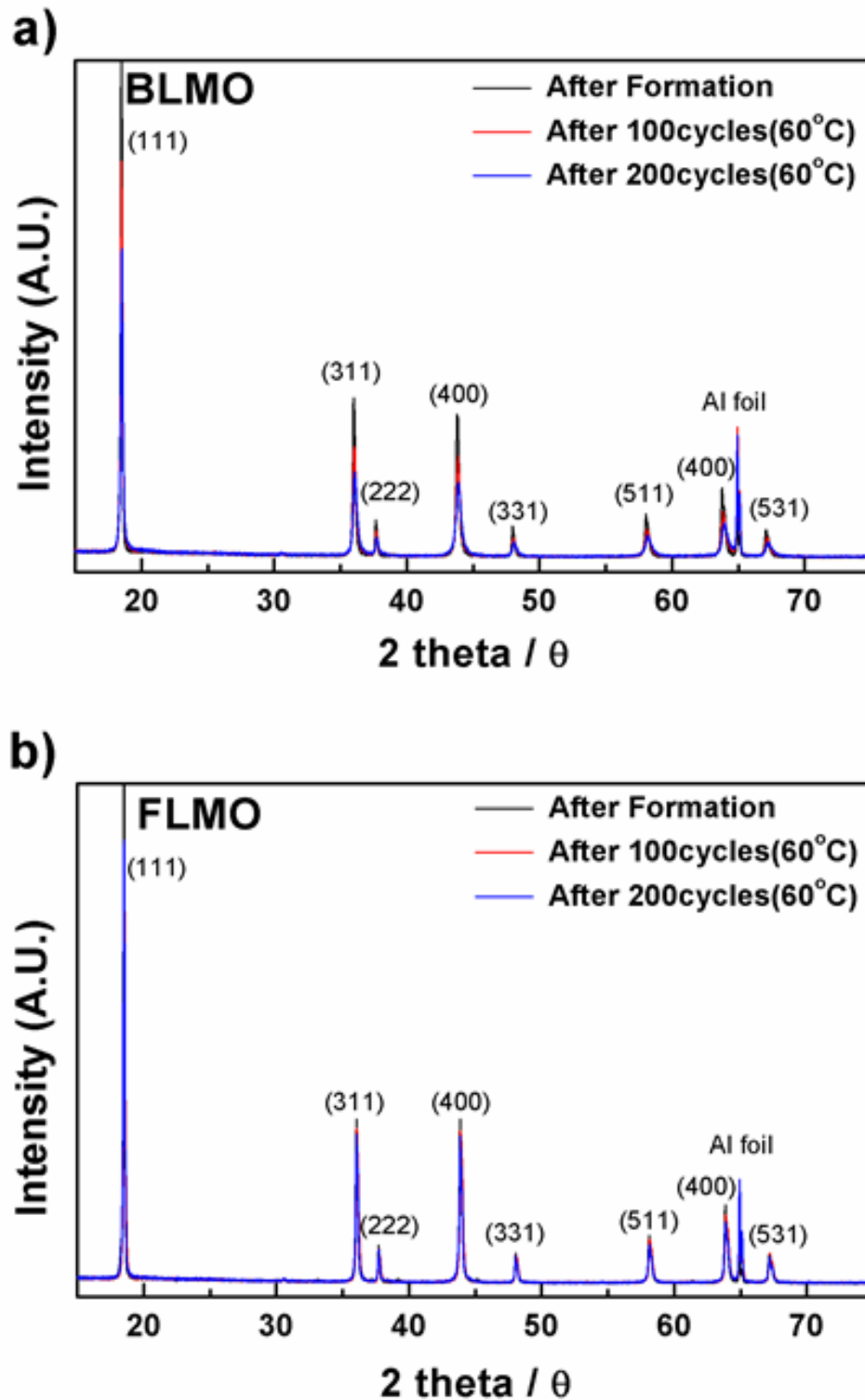


Figure 32. (a) Ex-situ XRD patterns of BLMO; before(black), after 100cycles(red), after 200cycles(blue) at 60°C (b) Ex-situ XRD patterns of FLMO; before(black), after 100cycles(red), after 200cycles(blue) at 60°C.

Table 3. The lattice parameter and the volume of the BLMO and FLMO.

Sample		Lattice parameter (Å)	Volume (Å ³)
BLMO	Formation	8.2249	556.41
	100cycle	8.2170	554.80
	200cycle	8.2084	553.06
FLMO	Formation	8.2148	554.36
	100cycle	8.2138	554.17
	200cycle	8.2133	554.06

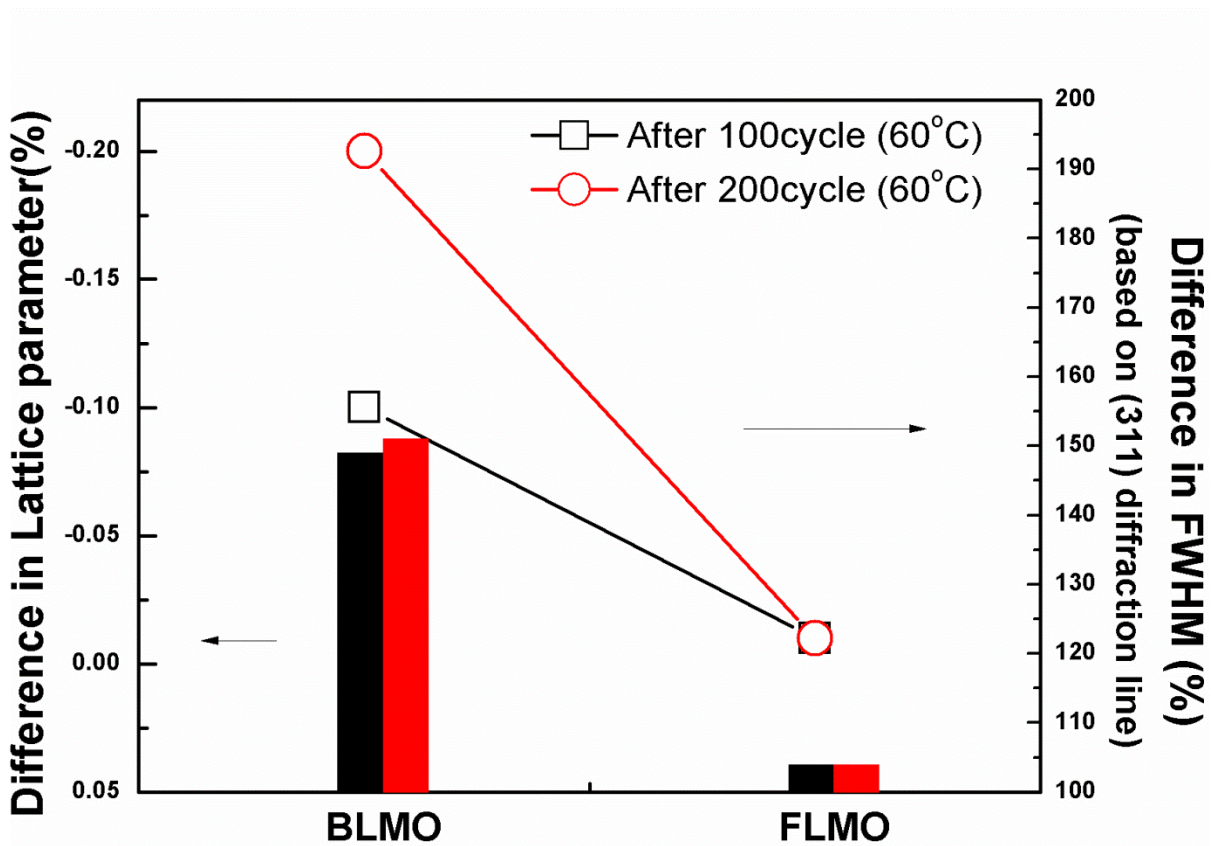


Figure 33. (a) Plot of difference in lattice parameter for samples after 100cycles(black) and 200 cycles(red) at 60°C (b) Plot of difference in FWHM based on (311) diffraction line for samples after 100cycles(black) and 200 cycles(red) at 60°C.

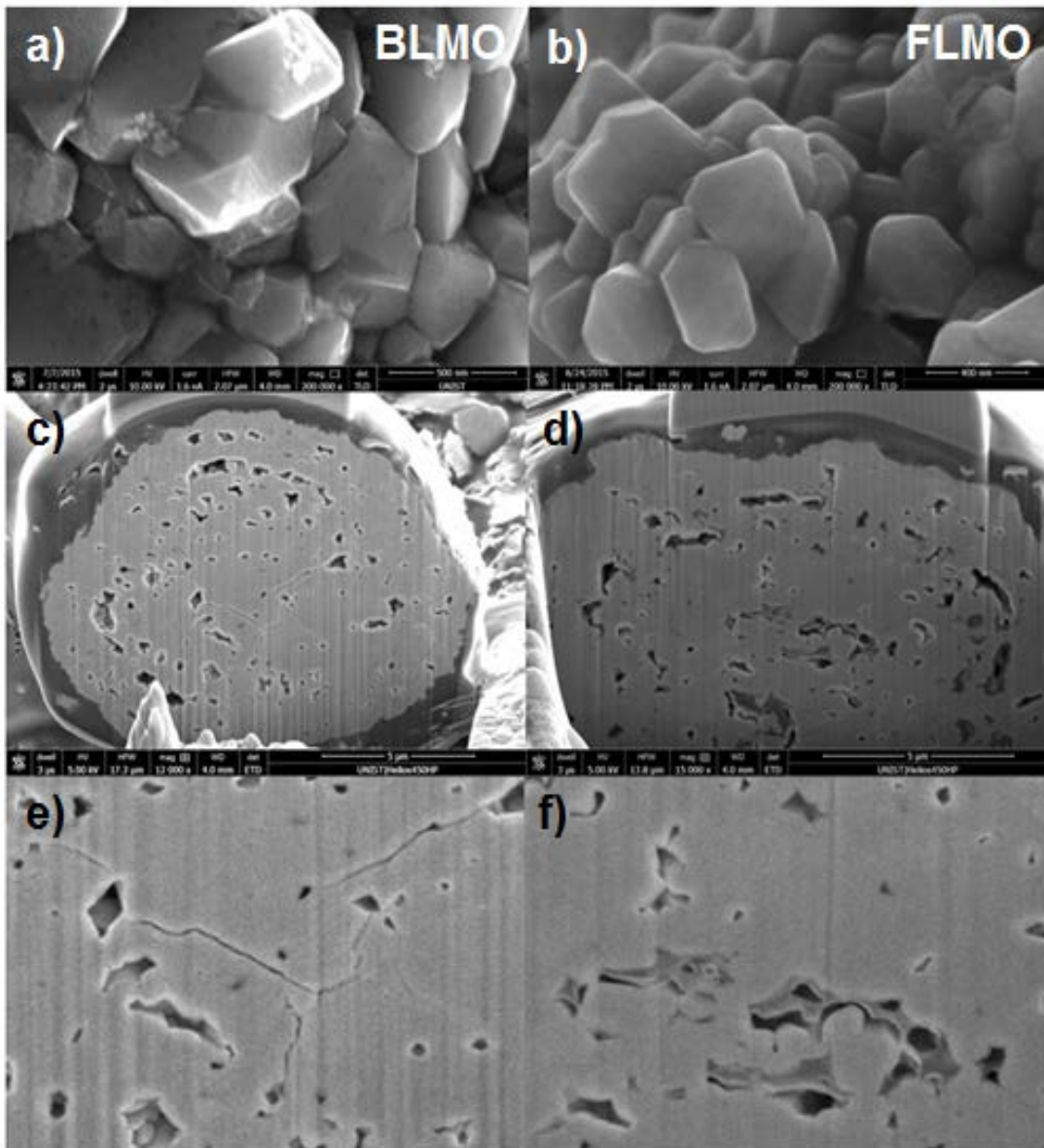


Figure 34. The SEM images of BLMO a) and FLMO b), particles after 100cycles at 60°C. The FIB-SEM images of the BLMO (c, e) and FLMO (d, f) after 100cycles at 60°C.

IV. Conclusion

In summary, the hetero-structure LiMn_2O_4 that has the thin layered phase formed on the surface of the spinel bulk phase was synthesized. The coexistence of the layered structure ($R\bar{3}m$) and spinel structure ($Fd\bar{3}m$) without forming any defect was confirmed via STEM analysis. And Mn-F bonds in the host spinel as well as surface film are stronger than Mn-O bonds. It leads to suppression of Mn dissolution. This newly developed material have high capacity and high stability at elevated temperature of 60°C as well as improved the charge-discharge rate capability compared to those of the BLMO.

REFERENCES

1. Larcher, D.; Tarascon, J. M., Towards greener and more sustainable batteries for electrical energy storage. *Nat Chem* **2015**, *7* (1), 19-29.
2. Tarascon, J. M.; Armand, M., Issues and challenges facing rechargeable lithium batteries. *Nature* **2001**, *414* (6861), 359-367.
3. Research, S., Cathode Material for Li-ion Secondary battery Technology Trend and Market Forecast. **2014**.
4. Park, O. K.; Cho, Y.; Lee, S.; Yoo, H.-C.; Song, H.-K.; Cho, J., Who will drive electric vehicles, olivine or spinel? *Energy & Environmental Science* **2011**, *4* (5), 1621-1633.
5. Lee, K. T.; Jeong, S.; Cho, J., Roles of surface chemistry on safety and electrochemistry in lithium ion batteries. *Accounts of chemical research* **2012**, *46* (5), 1161-1170.
6. Cabrera, S.; Benavente, F.; Vargas, M.; Flores, J. L.; Ortega, M.; Villca, J.; Mamani, R.; Leiva, N.; Luna, M.; Yapu, W., PERSPECTIVAS EN EL PROCESAMIENTO DE MATERIALES-ELECTRODOS PARA BATERÍAS DE ION LITIO EN BOLIVIA. *Revista Boliviana de Química* **2012**, *29* (1), 15-38.
7. Yoshio, M.; Noguchi, H.; Wang, H.; Wang, X., Correlation of oxygen deficiency with discharge capacity at 3.2 V for (LiMn)₃O_{4-z}. *Journal of power sources* **2006**, *154* (1), 273-275.
8. Myung, S.-T.; Komaba, S.; Kumagai, N., Enhanced Structural Stability and Cyclability of Al-Doped LiMn₂O₄ Spinel Synthesized by the Emulsion Drying Method. *Journal of The Electrochemical Society* **2001**, *148* (5), A482-A489.
9. Kannan, A.; Manthiram, A., Surface/Chemically Modified LiMn₂O₄ Cathodes for Lithium-Ion Batteries. *Electrochemical and Solid-State Letters* **2002**, *5* (7), A167-A169.
10. Ohzuku, T.; Kitagawa, M.; Hirai, T., Electrochemistry of Manganese Dioxide in Lithium Nonaqueous Cell III. X-Ray Diffractational Study on the Reduction of Spinel-Related Manganese Dioxide. *Journal of The Electrochemical Society* **1990**, *137* (3), 769-775.
11. Xu, B.; Meng, S., Factors affecting Li mobility in spinel LiMn₂O₄—A first-principles study by GGA and GGA+U methods. *Journal of Power Sources* **2010**, *195* (15), 4971-4976.
12. Tokura, Y.; Tomioka, Y., Colossal magnetoresistive manganites. *Journal of Magnetism and Magnetic Materials* **1999**, *200* (1-3), 1-23.
13. Huang, R.; Ikuhara, Y. H.; Mizoguchi, T.; Findlay, S. D.; Kuwabara, A.; Fisher, C. A.; Moriwake, H.; Oki, H.; Hirayama, T.; Ikuhara, Y., Oxygen-Vacancy Ordering at Surfaces of

Lithium Manganese (III, IV) Oxide Spinel Nanoparticles. *Angewandte Chemie International Edition* **2011**, *50* (13), 3053-3057.

14. (a) Whittingham, M. S., Lithium batteries and cathode materials. *Chemical reviews* **2004**, *104* (10), 4271-4302; (b) Xu, B.; Qian, D.; Wang, Z.; Meng, Y. S., Recent progress in cathode materials research for advanced lithium ion batteries. *Materials Science and Engineering: R: Reports* **2012**, *73* (5), 51-65.

15. Sickafus, K. E.; Wills, J. M.; Grimes, N. W., Structure of spinel. *Journal of the American Ceramic Society* **1999**, *82* (12), 3279-3292.

16. (a) Wang, X.; Nakamura, H.; Yoshio, M., Capacity fading mechanism for oxygen defect spinel as a 4 V cathode material in Li-ion batteries. *Journal of power sources* **2002**, *110* (1), 19-26; (b) Amatucci, G.; Schmutz, C.; Blyr, A.; Sigala, C.; Gozdz, A.; Larcher, D.; Tarascon, J., Materials' effects on the elevated and room temperature performance of CLiMn₂O₄ Li-ion batteries. *Journal of power sources* **1997**, *69* (1), 11-25; (c) Jang, D. H.; Shin, Y. J.; Oh, S. M., Dissolution of Spinel Oxides and Capacity Losses in 4 V Li/Li x Mn₂ O₄ Cells. *Journal of The Electrochemical Society* **1996**, *143* (7), 2204-2211; (d) Cho, I. H.; Kim, S.-S.; Shin, S. C.; Choi, N.-S., Effect of SEI on capacity losses of spinel lithium manganese oxide/graphite batteries stored at 60 C. *Electrochemical and Solid-State Letters* **2010**, *13* (11), A168-A172; (e) Thackeray, M., Structural considerations of layered and spinel lithiated oxides for lithium ion batteries. *Journal of The Electrochemical Society* **1995**, *142* (8), 2558-2563.

17. (a) Xia, Y.; Wang, H.; Zhang, Q.; Nakamura, H.; Noguchi, H.; Yoshio, M., Oxygen deficiency, a key factor in controlling the cycle performance of Mn-spinel cathode for lithium-ion batteries. *Journal of Power Sources* **2007**, *166* (2), 485-491; (b) Hao, X.; Lin, X.; Lu, W.; Bartlett, B. M., Oxygen Vacancies Lead to Loss of Domain Order, Particle Fracture, and Rapid Capacity Fade in Lithium Manganospinel (LiMn₂O₄) Batteries. *ACS applied materials & interfaces* **2014**, *6* (14), 10849-10857; (c) Lee, K.-S.; Myung, S.-T.; Jung, H.-G.; Lee, J. K.; Sun, Y.-K., Spinel lithium manganese oxide synthesized under a pressurized oxygen atmosphere. *Electrochimica Acta* **2010**, *55* (28), 8397-8401; (d) Takahashi, M.; Yoshida, T.; Ichikawa, A.; Kitoh, K.; Katsukawa, H.; Zhang, Q.; Yoshio, M., Effect of oxygen deficiency reduction in Mg-doped Mn-spinel on its cell storage performance at high temperature. *Electrochimica acta* **2006**, *51* (25), 5508-5514.

18. (a) Miura, K.; Yamada, A.; Tanaka, M., Electric states of spinel Li_xMn₂O₄ as a cathode of the rechargeable battery. *Electrochimica Acta* **1996**, *41* (2), 249-256; (b) Cho, J.; Thackeray, M. M., Structural changes of LiMn₂O₄ spinel electrodes during electrochemical cycling. *J. Electrochem. Soc.* **1999**, *146* (10), 3577-3581; (c) Yamada, A.; Tanaka, M.; Tanaka, K.; Sekai, K.,

- Jahn–Teller instability in spinel Li–Mn–O. *Journal of Power Sources* **1999**, 81–82, 73-78; (d) Yamada, A.; Tanaka, M., Jahn-Teller structural phase transition around 280K in LiMn₂O₄. *Materials Research Bulletin* **1995**, 30 (6), 715-721; (e) Thackeray, M. M.; Shao-Horn, Y.; Kahaian, A. J.; Kepler, K. D.; Skinner, E.; Vaughey, J. T.; Hackney, S. A., Structural Fatigue in Spinel Electrodes in High Voltage (4 V) Li/Li_xMn₂O₄ Cells. *Electrochemical and Solid-State Letters* **1998**, 1 (1), 7-9; (f) Shao-Horn, Y.; Hackney, S. A.; Kahaian, A. J.; Kepler, K. D.; Skinner, E.; Vaughey, J. T.; Thackeray, M. M., Structural fatigue in spinel electrodes in Li/Li_x[Mn₂]O₄ cells. *Journal of Power Sources* **1999**, 81-82, 496-499.
19. Wang, R.; Li, X.; Wang, Z.; Guo, H., Manganese dissolution from LiMn₂O₄ cathodes at elevated temperature: methylene methanedisulfonate as electrolyte additive. *Journal of Solid State Electrochemistry* **2015**, 1-10.
 20. Choa, J.; Thackeray, M. M., Structural Changes of LiMn₂O₄ Spinel Electrodes during Electrochemical Cycling. *Journal of The Electrochemical Society* **1999**, 146 (10), 3577-3581.
 21. Black, R.; Lee, J.-H.; Adams, B.; Mims, C. A.; Nazar, L. F., The Role of Catalysts and Peroxide Oxidation in Lithium–Oxygen Batteries. *Angewandte Chemie* **2013**, 125 (1), 410-414.
 22. Benedek, R.; Thackeray, M., Reaction energy for LiMn₂O₄ spinel dissolution in acid. *Electrochemical and solid-state letters* **2006**, 9 (6), A265-A267.
 23. Choi, M.; Kim, H.-S.; Kim, J.-S.; Park, S.-J.; Lee, Y. M.; Jin, B.-S., Synthesis and electrochemical performance of high-capacity 0.34 Li₂MnO₃·0.66 LiMn_{0.63}Ni_{0.24}Co_{0.13}O₂ cathode materials using a Couette–Taylor reactor. *Materials Research Bulletin* **2014**, 58, 223-228.
 24. Quinlan, F. T.; Sano, K.; Willey, T.; Vidu, R.; Tasaki, K.; Stroeve, P., Surface Characterization of the Spinel Li_xMn₂O₄ Cathode before and after Storage at Elevated Temperatures. *Chemistry of materials* **2001**, 13 (11), 4207-4212.
 25. Komaba, S.; Kaplan, B.; Ohtsuka, T.; Kataoka, Y.; Kumagai, N.; Groult, H., Inorganic electrolyte additives to suppress the degradation of graphite anodes by dissolved Mn(II) for lithium-ion batteries. *Journal of Power Sources* **2003**, 119–121, 378-382.
 26. Kanno, R.; Kondo, A.; Yonemura, M.; Gover, R.; Kawamoto, Y.; Tabuchi, M.; Kamiyama, T.; Izumi, F.; Masquelier, C.; Rousse, G., The relationships between phases and structures of lithium manganese spinels. *Journal of power sources* **1999**, 81, 542-546.
 27. (a) Kurata, H.; Lefevre, E.; Colliex, C.; Brydson, R., Electron-energy-loss near-edge structures in the oxygen K-edge spectra of transition-metal oxides. *Physical Review B* **1993**, 47 (20), 13763; (b) Koyama, Y.; Mizoguchi, T.; Ikeno, H.; Tanaka, I., Electronic structure of lithium nickel oxides by electron energy loss spectroscopy. *The Journal of Physical Chemistry B* **2005**,

109 (21), 10749-10755; (c) Kurata, H.; Colliex, C., Electron-energy-loss core-edge structures in manganese oxides. *Physical Review B* **1993**, *48* (4), 2102.

28. (a) Deng, B.; Nakamura, H.; Zhang, Q.; Yoshio, M.; Xia, Y., Greatly improved elevated-temperature cycling behavior of $\text{Li}_{1+x}\text{Mg}_y\text{Mn}_{2-x-y}\text{O}_{4+\delta}$ spinels with controlled oxygen stoichiometry. *Electrochimica Acta* **2004**, *49* (11), 1823-1830; (b) Lee, K. S.; Myung, S. T.; Jung, H. G.; Lee, J. K.; Sun, Y. K., Spinel lithium manganese oxide synthesized under a pressurized oxygen atmosphere. *Electrochimica Acta* **2010**, *55* (28), 8397-8401.

29. Tarascon, J. M.; Wang, E.; Shokoohi, F.; McKinnon, W.; Colson, S., The Spinel Phase of LiMn_2O_4 as a Cathode in Secondary Lithium Cells. *Journal of the Electrochemical Society* **1991**, *138* (10), 2859-2864.

30. Amarilla, J.; De Vidales, J. M.; Rojas, R., Electrochemical characteristics of cobalt-doped $\text{LiCo}_y\text{Mn}_{2-y}\text{O}_4$ ($0 \leq y \leq 0.66$) spinels synthesized at low temperature from $\text{Co}_x\text{Mn}_{3-x}\text{O}_4$ precursors. *Solid State Ionics* **2000**, *127* (1), 73-81.

31. Jiang, R.; Huang, Y.; Jia, D.; Wang, L.; Wang, L., High-Capacity, High-Cycling Cathode Material Synthesized by Low-Temperature Solid-State Coordination Method for Lithium Rechargeable Batteries $\text{Li}_{1+x}\text{Mn}_2\text{O}_{4-y}\text{F}_y$. *Journal of The Electrochemical Society* **2007**, *154* (7), A698-A702.

32. Han, D.-W.; Ryu, W.-H.; Kim, W.-K.; Eom, J.-Y.; Kwon, H.-S., Effects of Li and Cl Codoping on the Electrochemical Performance and Structural Stability of LiMn_2O_4 Cathode Materials for Hybrid Electric Vehicle Applications. *The Journal of Physical Chemistry C* **2013**, *117* (10), 4913-4919.

33. (a) Bang, H.; Donepudi, V.; Prakash, J., Electrochemical Performance of Al-doped LiMn_2O_4 Prepared by Different Methods in Solid-state Reaction. *Electrochim. Acta* **2002**, *48*, 443-451; (b) Feng, Q.; Kanoh, H.; Miyai, Y.; Ooi, K., Li^+ Extraction/Insertion Reactions with $\text{LiZn}_{0.5}\text{Mn}_{1.5}\text{O}_4$ Spinel in the Aqueous Phase. *Chemistry of materials* **1995**, *7* (2), 379-384; (c) Fu, Y.-P.; Su, Y.-H.; Lin, C.-H., Comparison of microwave-induced combustion and solid-state reaction for synthesis of $\text{LiMn}_{2-x}\text{Cr}_x\text{O}_4$ powders and their electrochemical properties. *Solid State Ionics* **2004**, *166* (1), 137-146.

34. (a) Kim, W.-K.; Han, D.-W.; Ryu, W.-H.; Lim, S.-J.; Kwon, H.-S., Al_2O_3 coating on LiMn_2O_4 by electrostatic attraction forces and its effects on the high temperature cyclic performance. *Electrochimica Acta* **2012**, *71*, 17-21; (b) Kim, Y. J.; Kim, T.-J.; Shin, J. W.; Park, B.; Cho, J., The Effect of Al_2O_3 Coating on the Cycle Life Performance in Thin-Film LiCoO_2 Cathodes. *Journal of The Electrochemical Society* **2002**, *149* (10), A1337-A1341; (c) Cho, J.; Kim, Y. J.; Kim, T.-J.; Park, B., Effect of Al_2O_3 -Coated LiMnO_2 Cathodes Prepared at

Various Temperatures on the 55° C Cycling Behavior. *Journal of The Electrochemical Society* **2002**, *149* (2), A127-A132.

35. (a) Lee, S.; Jeong, M.; Cho, J., Optimized 4-V Spinel Cathode Material with High Energy Density for Li-Ion Cells Operating at 60° C. *Advanced Energy Materials* **2013**, *3* (12), 1623-1629; (b) Liu, D.; He, Z.; Liu, X., Increased cycling stability of AlPO₄-coated LiMn₂O₄ for lithium ion batteries. *Materials Letters* **2007**, *61* (25), 4703-4706.

36. Arumugam, D.; Paruthimal Kalaigan, G., Synthesis and electrochemical characterizations of Nano-SiO₂-coated LiMn₂O₄ cathode materials for rechargeable lithium batteries. *Journal of Electroanalytical Chemistry* **2008**, *624* (1-2), 197-204.

37. Şahan, H.; Dokan, F. K.; Ülgen, A.; Patat, S., Improvement of cycling stability of LiMn₂O₄ cathode by Fe₂O₃ surface modification for Li-ion battery. *Ionics* **2013**, 1-11.

38. Sun, Y.-K.; Lee, Y.-S.; Yoshio, M.; Amine, K., Synthesis and Electrochemical Properties of ZnO-Coated LiNi_{0.5}Mn_{1.5}O₄ Spinel as 5 V Cathode Material for Lithium Secondary Batteries. *Electrochemical and Solid-State Letters* **2002**, *5* (5), A99-A102.

39. Gnanaraj, J.; Pol, V.; Gedanken, A.; Aurbach, D., Improving the high-temperature performance of LiMn₂O₄ spinel electrodes by coating the active mass with MgO via a sonochemical method. *Electrochemistry Communications* **2003**, *5* (11), 940-945.

40. Cho, J.; Kim, G. B.; Lim, H. S.; Kim, C. S.; Yoo, S. I., Improvement of Structural Stability of LiMn₂O₄ Cathode Material on 55° C Cycling by Sol-Gel Coating of LiCoO₂. *Electrochemical and Solid-State Letters* **1999**, *2* (12), 607-609.

41. Park, S.-C.; Kim, Y.-M.; Kang, Y.-M.; Kim, K.-T.; Lee, P. S.; Lee, J.-Y., Improvement of the rate capability of LiMn₂O₄ by surface coating with LiCoO₂. *Journal of power sources* **2001**, *103* (1), 86-92.

42. Liu, Z.; Wang, H.; Fang, L.; Lee, J. Y.; Gan, L. M., Improving the high-temperature performance of LiMn₂O₄ spinel by micro-emulsion coating of LiCoO₂. *Journal of Power sources* **2002**, *104* (1), 101-107.

43. Lee, M.-J.; Lee, S.; Oh, P.; Kim, Y.; Cho, J., High Performance LiMn₂O₄ Cathode Materials Grown with Epitaxial Layered Nanostructure for Li-Ion Batteries. *Nano Letters* **2014**.

44. Park, S.-C.; Kim, Y.-M.; Kang, Y.-M.; Kim, K.-T.; Lee, P. S.; Lee, J.-Y., Improvement of the rate capability of LiMn₂O₄ by surface coating with LiCoO₂. *Journal of Power Sources* **2001**, *103* (1), 86-92.

45. Lee, J.-W.; Park, S.-M.; Kim, H.-J., Effect of LiNi_{1/2}Mn_{1/2}O₂ coating on the electrochemical performance of Li-Mn spinel. *Electrochemistry Communications* **2009**, *11* (6), 1101-1104.

46. Park, S.-C.; Kim, Y.-M.; Han, S.-C.; Ahn, S.; Ku, C.-H.; Lee, J.-Y., The elevated temperature performance of LiMn₂O₄ coated with LiNi_{1-x}Co_xO₂ (X = 0.2 and 1). *Journal of Power Sources* **2002**, *107* (1), 42-47.
47. Lee, M.-J.; Lee, S.; Oh, P.; Kim, Y.; Cho, J., High performance LiMn₂O₄ cathode materials grown with epitaxial layered nanostructure for Li-ion batteries. *Nano letters* **2014**, *14* (2), 993-999.
48. Lee, S.; Yoon, G.; Jeong, M.; Lee, M. J.; Kang, K.; Cho, J., Hierarchical Surface Atomic Structure of a Manganese-Based Spinel Cathode for Lithium-Ion Batteries. *Angewandte Chemie International Edition* **2015**, *54* (4), 1153-1158.
49. Jeong, M.; Lee, M. J.; Cho, J.; Lee, S., Surface Mn Oxidation State Controlled Spinel LiMn₂O₄ as a Cathode Material for High-Energy Li-Ion Batteries. *Advanced Energy Materials* **2015**.
50. (a) Choi, W.; Manthiram, A., Superior capacity retention spinel oxyfluoride cathodes for lithium-ion batteries. *Electrochemical and solid-state letters* **2006**, *9* (5), A245-A248; (b) He, X.; Li, J.; Cai, Y.; Wang, Y.; Ying, J.; Jiang, C.; Wan, C., Fluorine doping of spherical spinel LiMn₂O₄. *Solid State Ionics* **2005**, *176* (35), 2571-2576; (c) Whitfield, P.; Davidson, I., Microwave Synthesis of Li_{1-x}Mn_{2-x}O₄ and Li_{1+x}Mn_{2-x}O_{4-y}F_y (x= 0.05, 0.15; y= 0.05, 0.1). *Journal of the electrochemical society* **2000**, *147* (12), 4476-4484; (d) Nguyen, C. C.; Bae, Y.-S.; Lee, K.-H.; Song, J.-W.; Min, J.-H.; Kim, J.-S.; Ko, H.-S.; Paik, Y.; Song, S.-W., Roles of fluorine-doping in enhancing initial cycle efficiency and SEI formation of Li-, Al-cosubstituted spinel battery cathodes. *Bulletin of the Korean Chemical Society* **2013**, *34* (2), 384-388; (e) Lee, H. R.; Lee, B.; Chung, K. Y.; Cho, B. W.; Lee, K.-Y.; Oh, S. H., Scalable synthesis and electrochemical investigations of fluorine-doped lithium manganese spinel oxide. *Electrochimica Acta* **2014**, *136*, 396-403.
51. Lee, J. H.; Hong, J. K.; Jang, D. H.; Sun, Y.-K.; Oh, S. M., Degradation mechanisms in doped spinels of LiM_{0.05}Mn_{1.95}O₄ (M= Li, B, Al, Co, and Ni) for Li secondary batteries. *Journal of power sources* **2000**, *89* (1), 7-14.
52. Zhu, H.-L.; Chen, Z.-Y.; Ji, S.; Linkov, V., Influence of different morphologies on electrochemical performance of spinel LiMn₂O₄. *Solid State Ionics* **2008**, *179* (27-32), 1788-1793.
53. (a) Wang, J.; Neaton, J.; Zheng, H.; Nagarajan, V.; Ogale, S.; Liu, B.; Viehland, D.; Vaithyanathan, V.; Schlom, D.; Waghmare, U., Epitaxial BiFeO₃ multiferroic thin film heterostructures. *Science* **2003**, *299* (5613), 1719-1722; (b) Hirayama, M.; Ido, H.; Kim, K.; Cho, W.; Tamura, K.; Mizuki, J. i.; Kanno, R., Dynamic structural changes at LiMn₂O₄/electrolyte

interface during lithium battery reaction. *Journal of the American Chemical Society* **2010**, *132* (43), 15268-15276.

54. Park, M.; Zhang, X.; Chung, M.; Less, G. B.; Sastry, A. M., A review of conduction phenomena in Li-ion batteries. *Journal of Power Sources* **2010**, *195* (24), 7904-7929.

55. (a) Bard, A. J.; Faulkner, L. R., *Electrochemical methods: fundamentals and applications*. Wiley New York: 1980; Vol. 2; (b) Shaju, K.; Rao, G. S.; Chowdari, B., Li ion kinetic studies on spinel cathodes, Li (M 1/6 Mn 11/6) O 4 (M= Mn, Co, CoAl) by GITT and EIS. *Journal of Materials Chemistry* **2003**, *13* (1), 106-113.

56. (a) Zhang, S.; Xu, K.; Jow, T., Understanding Formation of Solid Electrolyte Interface Film on LiMn₂O₄ Electrode. *Journal of The Electrochemical Society* **2002**, *149* (12), A1521-A1526; (b) Lei, J.; Li, L.; Kostecky, R.; Muller, R.; McLarnon, F., Characterization of SEI layers on LiMn₂O₄ cathodes with in situ spectroscopic ellipsometry. *Journal of the Electrochemical Society* **2005**, *152* (4), A774-A777.

57. (a) Xia, Y.; Zhou, Y.; Yoshio, M., Capacity Fading on Cycling of 4 V Li/LiMn₂O₄ Cells. *Journal of The Electrochemical Society* **1997**, *144* (8), 2593-2600; (b) Deng, B.; Nakamura, H.; Yoshio, M., Capacity fading with oxygen loss for manganese spinels upon cycling at elevated temperatures. *Journal of Power Sources* **2008**, *180* (2), 864-868.

VI. Acknowledgements

유니스트에 온지 엇그제 같은데 벌써 2년이라는 시간이 흘러서 졸업 하게 되었습니다.

먼저 부족한 저를 지도해주신 조재필 교수님께 감사드립니다. 교수님으로부터 많은 가르침을 받은 것 같습니다.

낯선 곳에 와서 많이 힘들 줄 알았는데 적응 잘 할 수 있게 챙겨준 모든 랩원분들께 감사드립니다.

그리고 무사히 석사생활을 마칠 수 있게 많은 가르침 주신 이민준오빠께 감사드립니다.

많은 동기들과 같이 입학해서 함께 대학원생활을 시작 하였는데 가장 먼저 졸업하게 되었네요. 좋은 추억 많이 만들어줘서 고맙고 다들 열심히 해서 좋은 성과 있길 바랄게요. 화이팅!!

마지막으로 교수님, 선배님들, 동기들, 후배들 진심으로 모두 다 행복하셨음 좋겠습니다.